Original Article

Modelling and verification of the nickel electroforming process of a mechanical vane fit for Industry 4.0

Eleni Andreou [1,*], Sudipta Roy

Electrochemistry & Corrosion Laboratory, University of Strathclyde, Chemical & Process Engineering, James Weir Building, 75 Montrose Street, Glasgow, G1 1XJ, United Kingdom

ABSTRACT

In previous studies, the comprehensive scaling-up of nickel electroforming on a lab-scale rotating disk electrode (RDE) suggested that secondary current distribution could adequately simulate such a forming process. In this work, the use of a 3-D, time-dependent, secondary current distribution model, developed in COMSOL Multiphysics®, was examined to validate the nickel electroforming of an industrial mechanical vane, a low-tolerance part with a demanding thickness profile of great interest to the aerospace industry. A set of experiments were carried out in an industrial pilot tank with computations showing that the model can satisfactorily predict the experimental findings. In addition, these experiments revealed that the local applied current density was related to the surface appearance (shiny *vs* matt) of the electroform.

Simulations of the process at applied current densities ≤ 5 A/dm^2 satisfactorily predicted the experimentally observed thickness distribution while, simulations of the process at applied current densities ≥ 5 A/dm^2 underpredicted the experimentally achieved thicknesses. Nevertheless, it is proposed that the model can be used for either quantitative or qualitative studies, respectively, depending on the required operating current density on a case-by-case basis. Scanning electron microscopy was used to determine the microstructure of the electroforms and determine the purity of nickel (*i.e.*, if nickel oxide is formed), with imaging suggesting that pyramid-shaped nickel particles evolve during deposition. Another interesting observation revealed a periodicity in the deposit's growth mechanism which leads to "necklace"-like deposit layers at the areas where the electroforms presented the highest thickness.

1. Introduction

The term "industrial revolution" is being used since 1837 (Blanqui, 1880) to describe highly influential, quick and deep socio-economic changes that take place over a period of time, effectively leading to industrial transitions. All three industrial revolutions so far had presented common characteristics which distinguish them from common, evolutional changes of the industrial sector (Fig. 1).

The main requirement for them to take place has always been the accumulation of various novel advances in the industrial production and any industrial revolution to follow will not be too much different. First, the competition among the new technological advances would ease quickly as, inevitably, quality will overtake quantity. Updated infrastructure will then be needed, the state and societies will evolve around

the transformed economy sector, new products and opportunities, production will be reorganised. As a result, the required resources and cost for production will be reduced, product quality will improve, niche products will be developed. Finally, the real sector of economy will reach a new development level (Popkova et al., 2019).

Following this model, a modern Fourth Industrial Revolution will require intense research and innovation in the fields of the Internet of Things (IT), Industrial Internet of Things (IIT) and Cloud and Smart Manufacturing (Vaidya et al., 2018).

Since the concept of "Industry 4.0" was introduced in 2011 (Slusarczyk, 2018), the most competitive industrial manufacturers around the world have been trying to secure the sustainability, high quality, and low cost of the fast technological developments of today. Using the continuously evolving and developing benefits that
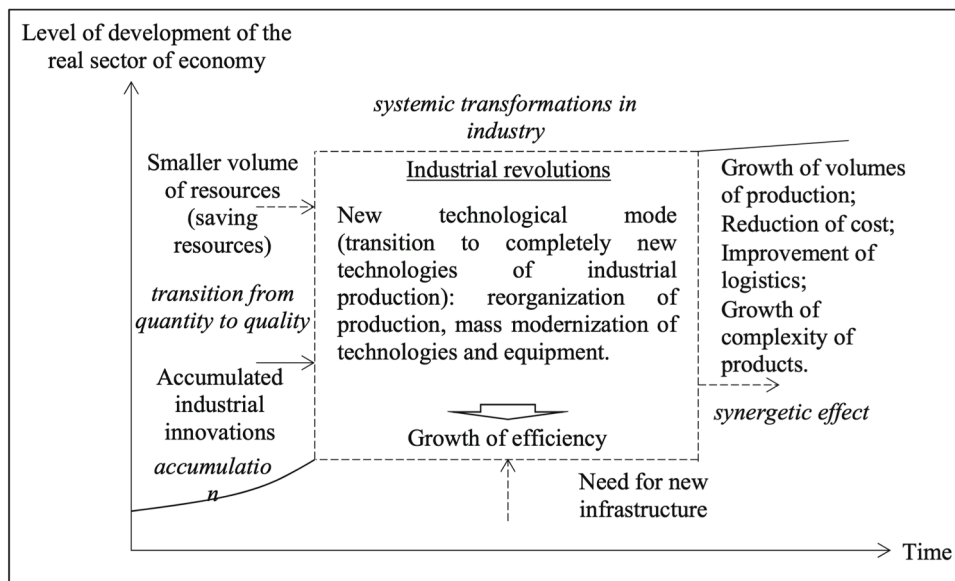
Fig. 1. Generalized model of an industrial revolution developed by Popkova et al. (2019).
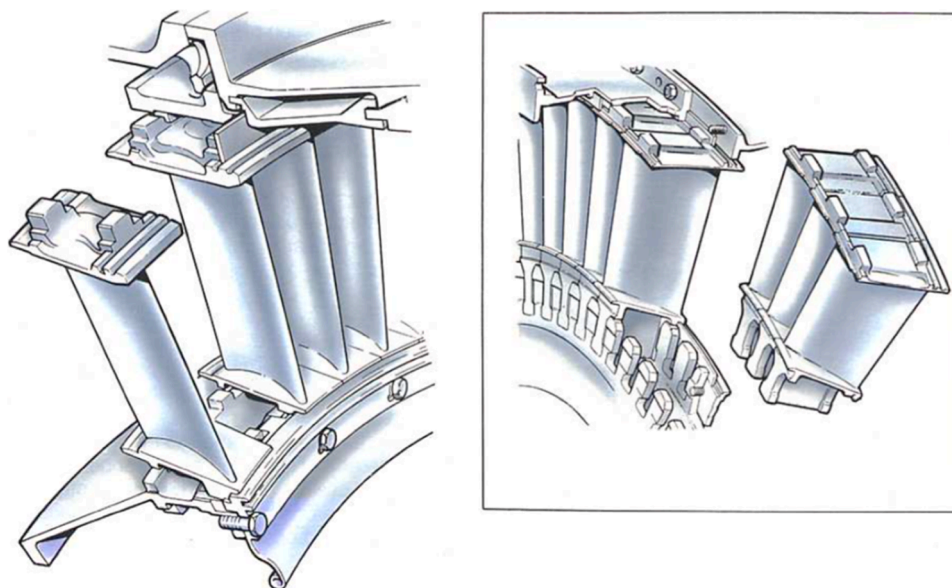

Fig. 2. Nozzle guide vanes detailed schematic (Rolls-Royce 1986).

cyber-physical systems, the internet of things and artificial intelligence have to offer, the total computerisation of manufacturing and fabrication has been set as the greater aim (Müller et al., 2018). While the three pillars of "Industry 4.0" mentioned above take care of the conversion of experimental data into digital format, to establish the smart factories of the future, processes themselves need to enter a new era. As a result, new manufacturing technologies arise every day aiming to replace traditional production lines with more flexible ones, able to support the evolved industrial needs during the next industrial transition.

Among those technologies, additive manufacturing (AM) processes are gaining ground (Ford and Despeisse, 2016) due to their potential to transform production of parts for the "low-volume / high-value" industrial sectors, such as the aerospace and marine industries. One of the most appealing characteristics of AM techniques is the producer-client relationship that could be enabled through data transfer. The extensive use of software tools provides both customers and producers with the ability to digitally preview the customised product, enabling

efficient design of tooling and production (Berman, 2012; Chen et al., 2015; Huang et al., 2013; Petrick and Simpson, 2013; Petrovic et al., 2011). Moreover, the development of new products could move at a faster pace, providing industry with the ability to manufacture novel products of complex shapes and geometries (Ford and Despeisse, 2016), such as those encountered by electroforming.

Electroforming was first introduced to the scientific society by the Prussian engineer and physicist, Moritz Hermann von Jacobi, in 1838. Since then, by being used in applications from micro-components for the medical and electronics industries to aircrafts and various aero-structures, this AM process has been impacting our daily life in different ways (Parkinson, 1998). However, it remains, up to this day, a manufacturing process that scientists, researchers, and engineers do not know much about, mostly because the majority of the scientific investigations are only conducted by companies that already use it in their production lines and, consequently, the results remain confidential for years (or even forever). This is the case predominantly for research
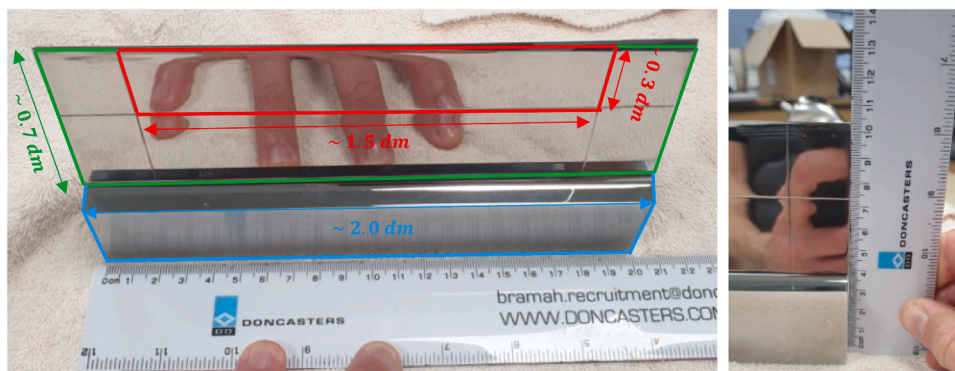
Fig. 3. Vane mandrel made of 304 stainless stell provided by the industry partner for research and development of a real-life product. The area in red is always electroformed, the area in green may be masked or electroformed, the area in blue is always masked.
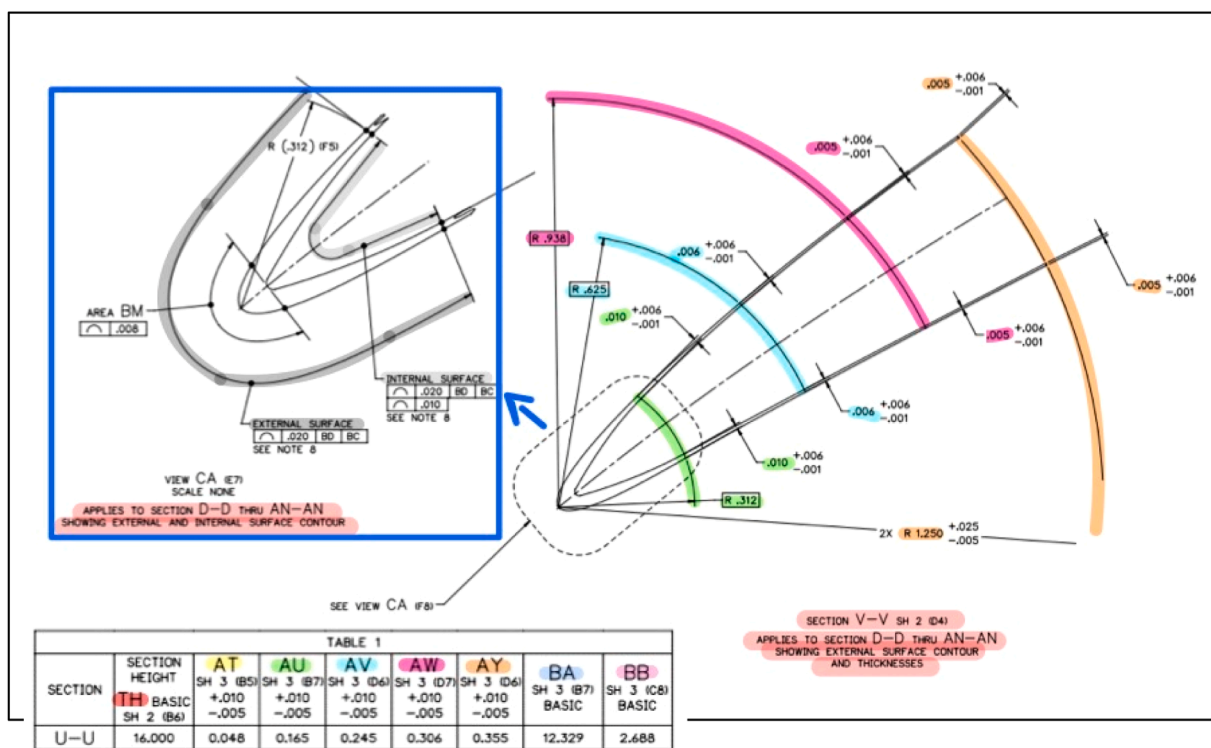

Fig. 4. Schematic of the vane mandrel geometry profile showing the thickness target along different sections of the part.

Table 1

Thickness target for the different sections of the vane mandrel. Nominal thickness targets and tolerances are provided.

Thickness Target (mm)					
Part Section	AT ("nose")	AU	AV	AW	AY (end boundary)
Nominal	1.2192	0.254	0.1524	0.127	0.127
Tolerance	0.254	0.1524	0.1524	0.1524	0.1524
	−1.27	−0.0254	−0.0254	−0.0254	−0.0254
Minimum	1.0922	0.2286	0.127	0.1016	0.1016
Maximum	1.4732	0.4064	0.3048	0.2794	0.2794

related to the "heavy" industries, such as the automotive and aircraft/aerospace ones. In both these sectors, electroforming is most usually used to fight corrosion, alongside wear-resistance and durability improvements. Nickel is the most electroplated metal in these industries, due to its significant mechanical and anti-corrosion properties.

In the aerospace industry, specifically, the various types of metal deposition have been proved to be the most promising among the AM processes to meet the quality challenges of the sector (Uriondo et al., 2015), with the most famous among them being the electroforming of nickel. Therefore, their continuous study, characterisation and optimisation is of the utmost importance; airworthiness and air transport safety must be guaranteed with no space for errors of any kind. Corrosion-resistance at high temperatures, protection against abrasion and erosion (Watson, 1990), development of advanced tooling and increase of repairability rates are only few of the reasons which justify the viable role that electroforming plays for this industrial sector. In some cases, (nickel) electroforming is even the only practical and cost-efficient way to produce specific parts such as, parts used in electromagnetic interference shielding, volume compensators and temperature and pressure sensors (Parkinson, 1998).

Mechanical vanes (Fig. 2) are among the aerospace applications that can benefit from the use of electroforming as their fabrication process. In general, mechanical vanes play an integral role in gas turbine engine
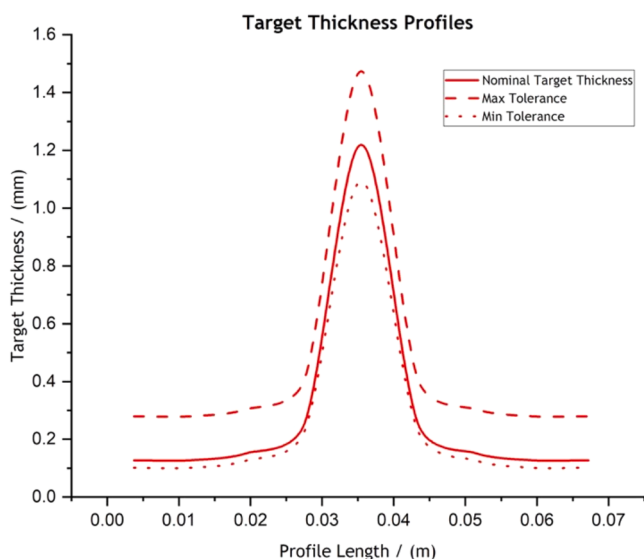
Fig. 5. Thickness profiles of the minimum (dotted line), nominal-target (straight line) and maximum (dashed line) acceptable thicknesses for each section.

design and, therefore, are of great industrial interest. Since their main function is to guide and optimise the air flow as the fluid moves through the engine, their design must abide by strict profile and thickness requirements, followed by low tolerances during manufacturing (Madhwesh et al., 2011; Goel et al., 2008; Hogner et al., 2016). As near net shape parts, vanes are an interesting challenge for the electroforming process.

Potentially allowing for a lower-cost, energy-efficient and lower-waste fabrication compared to traditional methods (*e.g.*, casting, hot isostatic pressing), as well as more controllable and stress-free deposition with minimal or zero post-processing requirements, the optimisation of the nickel electroforming of such parts is crucial before scaling up. However, up to this date, most optimisation efforts primarily rely on empirical knowledge, which currently constrains transformation into high volume manufacturing due to the high cost and risk of any potential practical scaling up tests.

To overcome this limitation, the construction of reliable modelling tools that can simulate the electroforming process could be of significant value and has been extensively discussed in a previous work (Andreou and Roy, 2021). Starting from the study of the system's geometry, developing an accurate picture of process chemistry and electrode kinetics, as well as including other transfer phenomena, a reliable model can be built to reveal the process's inherent weaknesses and strengths and assist in the effort to optimise it.

The interest in simulating the electroforming process is not a demand of modern times. The first numerical studies of the process made their appearance in the 1970s. In 1978, Alkire et al. (1978) published a systematic 2-D study of a shape evolution problem, assuming secondary current distribution, using the finite element method (FEM) to conclude that this numerical approach proves to be reliable, rather limitless, and flexible in modelling current distribution problems. Even though they reported difficulties in modelling both the potential field and the outward growth close to a singularity, the researchers suggested that the use of the finite element method could play an important role in solving complex electrochemical boundary problems. Following a long period after Alkire's study, Masuku et al. (2002) applied FEM in 2002, to develop, compare and validate 2-D and 3-D models of an electroplating process based on industrial data using the ANSYS simulation software. In a study of great interest to industry they reported that the current flow between the electrodes is of a 3-D nature which, in turn, reduces the electrical resistance in the electrolyte and increases the current when

compared to the 1-D and 2-D models. By validation through experiments, they established that 2-D modelling is not reliable when it comes to simulation modelling of industrial processes, suggesting that the optimisation of 3-D models is of essence for their efficient modelling. Other studies by Oh et al. (2004) in 2004 and Yang et al. (2008) in 2005 investigated and confirmed the significant effect of the system's geometry on the current distribution and, consequently, on current and thickness uniformity. The researchers, however, suggested that further current distribution studies need to be carried out for optimum results to be achieved. Finally, one of the most recent and comprehensive electroforming studies, is the one published by Heydari et al. (2020) in 2020 discussing the modelling of copper deposition on an aluminum conical rotating electrode, using COMSOL Multiphysics®. The effect of current density, electrolyte conductivity, and electrode placement on the process were investigated and modelling predictions were validated against experiments. They reported that the distance between the electrodes, as well as their sizes, significantly affect thickness uniformity. Specifically, the process was determined to be more efficient and the thickness more uniform when the anode and cathode were the same size. At the same time, the distance between the electrodes affected both process efficiency and deposit quality and therefore, the need to determine an optimum distance among the electrodes was established.

As part of the authors' aspiration to put together some of the missing pieces of previous studies and follow up on investigations that were reported as inconclusive, this work - the fourth in a series of relevant papers - presents the experimental and modelling studies conducted as part of an attempt to predict the growth of an electroformed part in a real process. Even though a complete model of the nickel electroforming process, of different scales, has already been developed and discussed in one of the earlier papers in the series (Andreou and Roy, 2022), the mandrel geometries in that investigation were simple, which are rarely encountered in industry. In that work, it was also shown that secondary current distribution was sufficient to predict qualitatively and quantitatively nickel deposition and growth. Starting from that base model, here, a 3-D model of a mechanical vane was developed and successfully validated, in terms of deposit thickness, against deposition experiments in a prototype electroforming reactor (Andreou and Roy, 2022). First, a qualitative analysis of experimental results was carried out to determine process characteristics such as the deposition rate and the direction in which material deposition takes place on the surface, as well as to determine the process predictability.

Moving forward, simulations of deposition at current densities up to 7.22 A/dm^2 were run and validated against experimentally achieved thicknesses. Attention was especially focused on the rates at which deposition evolves both at the tip of the vane and at its side faces to determine whether industry requirements for a thick tip against thinner sides could be met. The last part of the investigation included the microstructural characterisation of the electroformed vanes. Scanning electron microscopy was utilised to determine the growth mechanism of the deposited nickel layers over the duration of the process while elemental analysis was carried out to determine deposit uniformity and composition.

Following that approach, the authors believe that this work provides a good example of how research could be highly relevant and beneficial to "Industry 4.0", combining systematic experimental studies focused on process optimisation with the integration of advanced digital tools.

2. Materials & methods

For the experimental and simulation studies presented here, our industry partner provided a modified 304 stainless steel mandrel of a mechanical vane (Fig. 3). The geometry of this vane mandrel presented a challenging profile, with precision curves which could be very difficult (if possible, at all) to be developed by any other traditional metal manufacturing process (*e.g.*, forging or casting).

Fig. 6. **(a)** The complete protype electroforming setup in the UoS workshop, **(b)** the anode basket filled with nickel pellets in the tank, **(c)** view of the filled tank with the titanium anode basket and a stainless-steel mandrel.

With reference to Fig. 3, the area in red (inside of the scribed lines) is always required to be electroformed while the area in green may be masked or electroformed and the area in blue should always be masked. Keeping in mind that there are two faces on the mandrel, and assuming that the curvature area at the "tip" is negligible, the total electroforming area is $A_{vane} = \sim 0.9$ dm^2 (both sides), allowing for a trim allowance area of ~ 1.9 dm^2, out of the total mandrel area of ~ 2.8 dm^2. The challenging profile of this mandrel is evident by the schematics shown in Fig. 4. The design requirements suggest that the part should present a changing profile in terms of thickness, starting from a thicker deposit of 1.2192 mm nominal at the tip, or "nose" (section AT), and transitioning to a thinner deposition of 0.127 mm nominal close to the geometry end boundary (section AY). For the part sections in between, section AU, section AV and section AW, the nominal target thicknesses are identified at 0.254 mm, 0.1524 mm and 0.127 mm, respectively.

The detailed thickness profile transition requirements, as well as the acceptable tolerance, are presented in Table 1. The colour code used to identify the part sections of different thicknesses in Fig. 4 is also used in Table 1 for easy identification of the corresponding thickness targets.

Fig. 5 shows a plot of the thickness profiles corresponding to the minimum, nominal (target) and maximum thicknesses acceptable for each part section, as prescribed by industry. One is expected to meet these tolerances during electroforming.

It is important to note here that the thickness targets and tolerances provided in Table 1 have been provided by Radius Aerospace to represent targets that are usually required by customers.

To cross-validate model predictions against practical experiments of a similar industrial-scale setup, a polypropylene (PP) 18 L electroforming tank was designed by the authors and manufactured by PolyPlas Engineering Ltd. Fig. 6a shows the complete, prototype electroforming tank setup at the UoS industrial workshop.

The system used a SIEBEC MC15 pump and filter system to achieve sufficient electrolyte circulation. The M15 magnetic drive pump allowed for a maximum flowrate of 1.5 m^3/h, while particles of even 0.5 μm were filtered using an on-line filter. A SIEBEC polypropylene 1⁄4" eductor nozzle was used to circulate the electrolyte within the tank. The electrolyte was heated by a 0.5 kW BRAUDE Polaris cylindrical non-corrodible heater. A BRAUDE Tankmaster MP temperature and level controller was used for continuous monitoring and controlling of the solution.
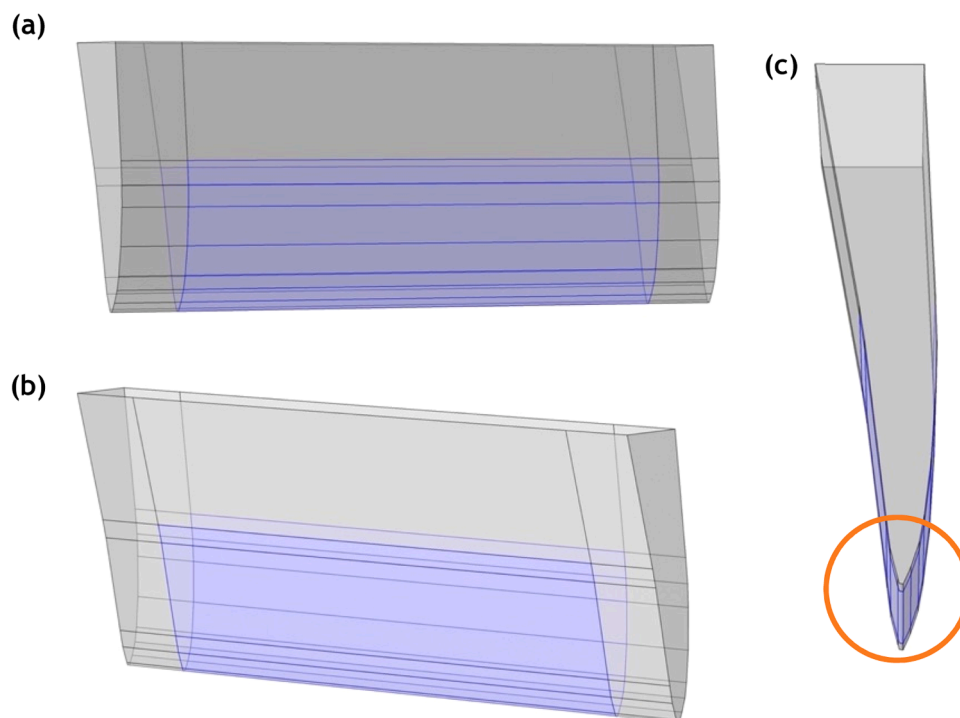
Fig. 7. 3-D geometry of the mechanical vane mandrel used in COMSOL Multiphysics®. **(a)** Front and **(b)** back views of the deposition area. **(c)** Side view of the mandrel revealing the challenging profile of the tool. The "nose" of the mandrel indicated in the circle.
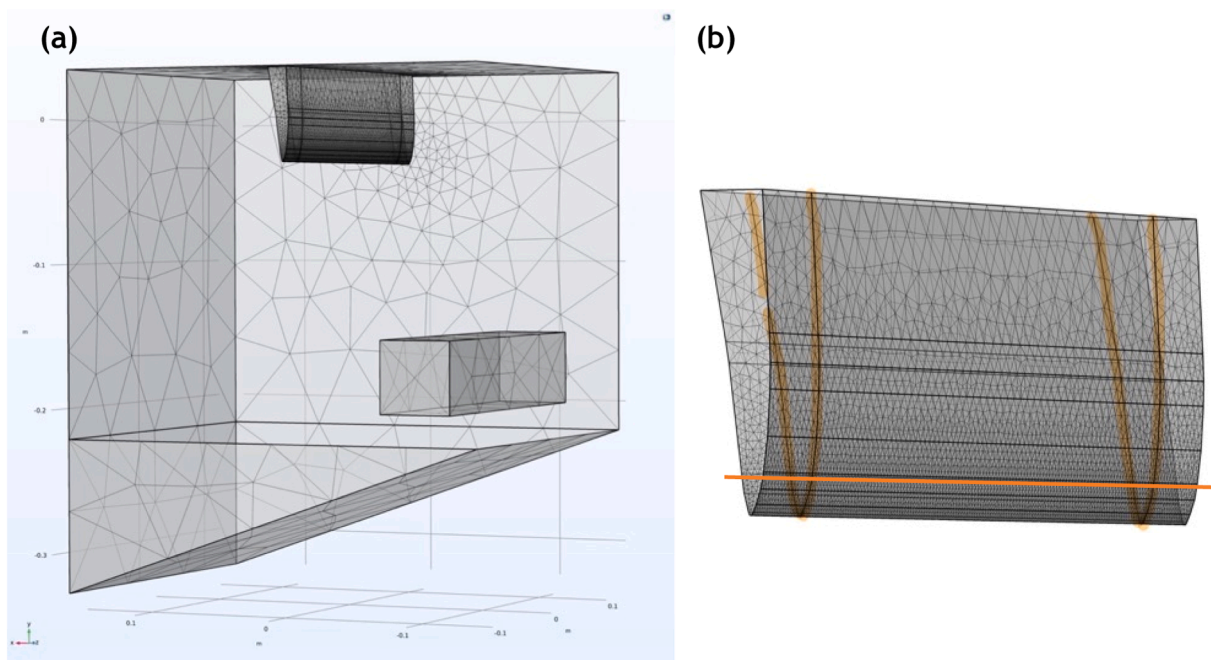

Fig. 8. Mesh spacing of **(a)** the whole 3-D mechanical vane model domain and **(b)** the whole mandrel area.

Table 2
User-defined, general and boundary, user-defined, element size parameters for both the RDE and scaled-up models.

Element Size Parameters	General	"Nose"	Rest of Cathode
Maximum Element Size (mm)	100	1.5	5
Minimum Element Size (mm)	1	–	–
Maximum Element Growth Rate	1.3	1.1	1.1

A titanium basket filled with industrial grade nickel pellets (Fig. 6b) was used as the anode. The 304 stainless steel mandrel used as the cathode was provided by Radius Aerospace. The electrodes were immersed in the nickel sulphamate-based electrolyte by mounting them on 12 mm copper busbars of > 99 % purity (Fig. 6c). Current was applied by a 20 A, 18 V RS PRO Switching DC Power Supply using 30 A, steel, BU- 65-0 Farnell crocodile clips.

Table 3
Model physical and (electro)chemical input parameters.
Detailed calculations available in the Supplementary Material.

	Parameter	Model	Comments
Electrolyte	Temperature	323 K	User defined (50°C)
	Electrolyte conductivity	0.9165 S/dm	From Experimental Data
Electrodes	Dissolving-depositing species	Mr_{Ni} = 0.05869 kg/mol ρ = 8.908 kg/l	From literature
	Number of participating electrons	n = 2	$Ni \rightarrow Ni^{2+} + 2e^-$
	Stoichiometric coefficients for dissolving-depositing species	1	$Ni \rightarrow Ni^{2+} + 2e^-$
	Equilibrium potential	E_{eq} = − 0.52 V	Reversible Potential from Experimental Data
	Exchange current density	$i_{0,m}$ = 0.42 A/dm²	From Experimental Data
	Anodic transfer coefficient	$\alpha_{a,m}$ = 1.806	From Experimental Data
	Cathodic transfer coefficient	$\alpha_{c,m}$ = 0.194	From Experimental Data
	Limiting Current Density	$i_{lim,m}$ = 208.138 A/dm²	From Experimental Data

Table 4
Process parameters of the deposition experiments conducted in the electro-forming tank reactor using the mechanical vane mandrel.

Deposit	Applied Current (A)	Current Density (A/dm²)	Duration (h)	Deposit Mass (g)
R1	1	1.11	5	5.4
R2	2.2	2.44	5	10.39
R3	4.4	4.89	5	19.79
R4	4.4	4.89	2.5	12
R5	6.5	7.22	3.5	19.5
R6	6.5	7.22	5	30.856
R7	6.5	7.22	6	41.363

3. Model development

A time-dependent 3-D model of the mechanical vane system was developed within the *Electrodeposition* module of *COMSOL Multiphysics®* following a methodology that has been fully described in an earlier paper, plating on a disk at two different scales, *i.e.*, laboratory scale and piloting scale (Andreou and Roy, 2022). Both the experimental and modelling studies of the mechanical vane geometry were conducted considering the deposition area to be the one indicated in red in Fig. 3, while the rest of the mandrel area was kept masked. Fig. 7 below shows the mandrel geometry as introduced in the modelling software. Here, the front (Fig. 7a) and back (Fig. 7b) view of the mandrel are provided, with the deposition area indicated in blue. Throughout this chapter, "front" indicates the mandrel face closer to the anode. In the circle, the tip of the mandrel, also referred to as the "nose", is highlighted.

Fig. 7c shows the side view of the mandrel which reveals the challenging curved profile of the tool which is described in *Section 2*.

A user-defined mesh spacing was chosen for the vane model (Fig. 8a). This included 164,759 elements with minimum element quality of 0.2108 and an average element quality of 0.6564. Once more, the mesh

on the cathode boundary was the finest (Fig. 8b). The meshing parameters are provided in Table 2. The area below the orange line in Fig. 8b indicates what was considered to be the "nose" area. Because of the significantly intense curvature of the mandrel's tip, the mesh spacing there had to be extremely fine to avoid convergence issues due to inverted mesh elements. The rest of the mandrel area was spaced using a smooth increase in mesh element size while the remaining geometry, including the anode boundary, was spaced based on the general parameters provided in Table 2. The mesh was mainly made up of tetrahedrals, with some triangular elements also used to optimise mesh spacing close to challenging edges, like the ones enclosing the deposition area and highlighted in orange in Fig. 8b.

Secondary current distribution (SCD) was once more chosen to describe the problem physics. The electrochemical input parameters are provided in Table 3 were used for the development of the mechanical vane model.

4. Results & discussion

4.1. Experimental results

Nickel deposits were formed under various experimental conditions to assess both the predictability and consistency of the process. Table 4 summarises the details of the experiments conducted in the electro-forming tank reactor using the mechanical vane mandrel (cathode). The electroforms were developed in a nickel sulfamate electrolyte while a sacrificial nickel anode was employed, always kept at least double in surface area compared to the cathode one, to avoid any of the potentially complicated passivation phenomena that can be observed in electrolytes with sulfur content (Green et al., 2022). The equivalent mass of the deposited nickel presented here include the dendritic growth area around the leading edges, since the dendrites contribute towards current consumption.

As it can be concluded based on the information shown in Table 4, the process results are predictable. Doubling the applied current density and keeping the deposition time the same leads to an almost double deposited nickel mass (compare electroforms R1 & R2, R2 & R3). The same behaviour is observed if deposition duration is doubled while the applied current density remains the same (compare electroforms R5 & R7). At the same time, if both the applied current density and deposition duration are halved the deposited nickel mass will remain approximately the same (compare electroforms R2 & R4).

Through a closer inspection of electroforms R5, R6 and R7, which are shown in Fig. 9, someone can determine the growth rate of the process in terms of depositing nickel mass. By keeping the current density at 7.22 A/dm², deposition for 3.5 h leads to a growth rate of ∼ 5.57 g/h (R5), deposition for 5 h leads to a growth rate of ∼ 6.2 g/h (R6) while, deposition for 6 h leads to a growth rate of ∼ 6.9 g/h (R7).

These results suggest an average process growth rate of ∼ 6.2 g/h. Since all deposits were weighted as a whole, including the dendritic growth around their leading edges, the small differences in the deposited nickel mass among the three deposits is attributed to the different dendrite sizes observed. The dendrites observed around electroform R5 are considerably thinner than the ones observed around electroforms R6 and R7, in order of increasing dendrite size, as it is shown in Fig. 9.

On another front, the systematic experimental approach revealed a correlation between the applied current density and the electroforms' surface finishing. As it can be seen in Fig. 10, electroforms R1 and R2 which were produced by deposition at 1.11 A/dm² and 2.44 A/dm², respectively, for 5 h, presented a shiny surface finishing while, electroform R4 which was produced by deposition at 4.89 A/dm² for 2.5 h, presented a matte surface finishing. Interestingly enough, electroform R3, produced by deposition at 4.89 A/dm² for 5 h, presented a matte surface finishing at the sides and a shiny one in the middle.

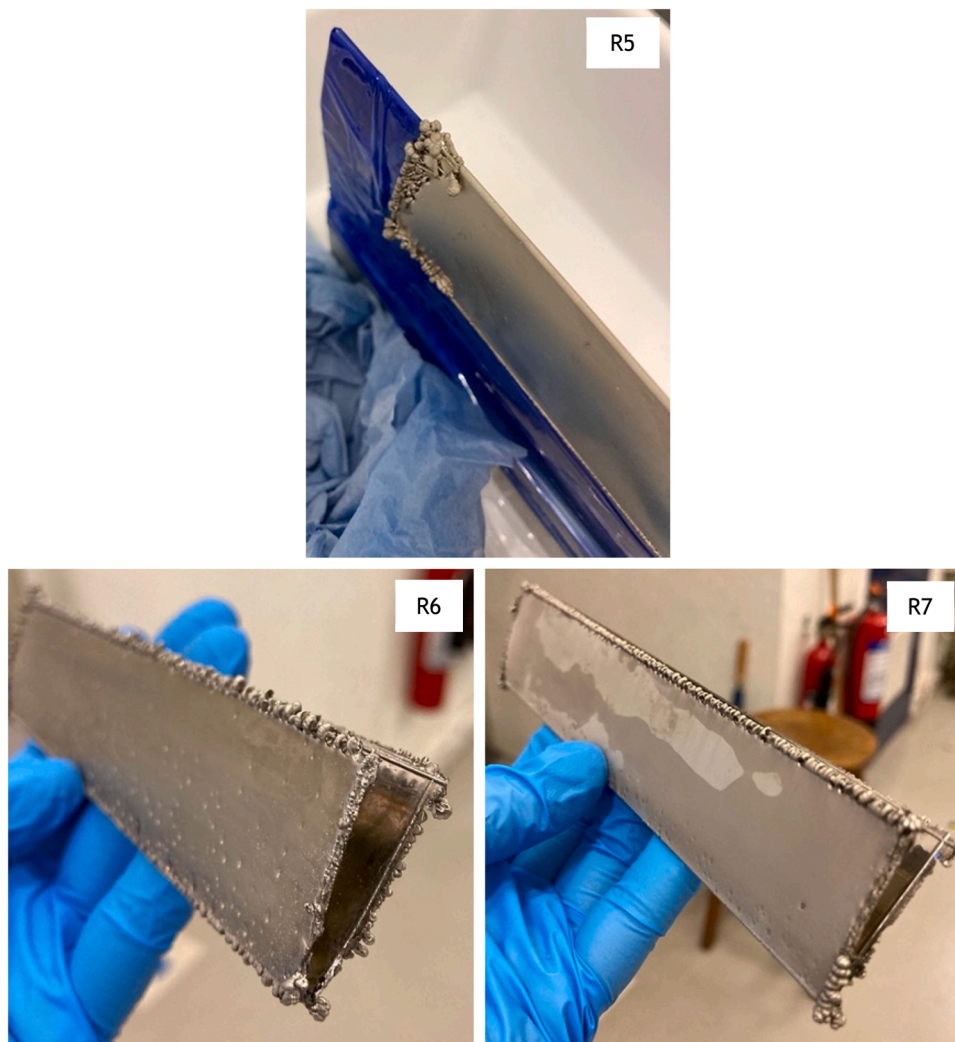A surface with little or no roughness allows only a small range of

Fig. 9. Nickel mechanical vane electroforms R5, R6 and R7. The difference in the dendrites size is highlighted, with R5 presenting the thinnest dendrites around its leading edges and R7 the thicker ones. Electroforms R5, R6 and R7 were produced at 7.22 A/dm² after deposition for 3.5 h, 5 h and 6 h, respectively, at 50 °C.

incident directions for which light can be reflected toward a point of observation, resulting in these surfaces being identified as shiny ones by an observer (Todd and Norman, 2018). Since shiny surfaces are observed either at lower current densities, or after deposition at higher current densities for shorter periods, these observations suggest that the first layers are deposited on the cathode creating a smooth which appears shiny. As more layers are being deposited, either because of faster deposition at higher current densities, or because of longer deposition periods even at lower current densities, the surface roughness increases hence the surface appears with a matte finishing.

As a general comment, the qualitative analysis of the surface appearance of electroforms discussed here indicates that deposition progresses from the sides of the cathode towards the middle of it. The faster deposition rate at the sides of the mandrel is also confirmed by the thickness distribution studies carried out for the vane electroforms and which are discussed in detail in the following section.

4.2. Model results

The simulations discussed in this chapter were designed to represent practical deposition experiments, at 50 °C, for 5 h, when the cell voltage lies at 5.4 V and deposition is conducted at a current density of $\sim$ 4.8 A/dm². To achieve that, the cathode phase condition was described by a total applied current $I_{l,total} = -4.4$ A and an applied boundary electric potential $\varphi_{s,ext,init} = -5.4$ V, while the anode boundary was described by an applied boundary electric potential $\varphi_{s,ext} = 0$ V to represent a cell voltage at 5.4 V.

Fig. 11 shows the current and potential distribution results after the simulation had converged. The simulations suggested a potential range within the electrolyte of -1.64 V to 0.51 V (Fig. 11) and a current density range between 3.32 A/dm² and 2.28×10^4 A/dm² (Fig. 11). The current lines are shown here to, once more, bend away from the insulator walls since no current can pass through them, travelling towards the cathode surface and concentrating specifically around the "nose". These results agree with what is observed in practice; the vane deposits always present higher thicknesses at the "nose" compared to the remaining deposition surface.

Subsequently, Fig. 12 presents the simulated deposit thickness distribution. Since the current is predicted to be higher at the edges and the "nose", a higher thickness was predicted at these areas. The range of the predicted thickness lies at an average of $0.2 - 0.45$ mm, with the values reaching 0.45 mm closer to the leading edges and the "nose". In Fig. 12 only the front face of the mandrel is shown just for visualisation purposes. Detailed numerical graphs follow as part of the model validation below. To validate the modelling results deposit R3 (Fig. 13) was used. The experimental conditions applied to form this deposit were the same as the ones chosen for the simulations above (-5.4 V and -4.4 A, for 18000 s).
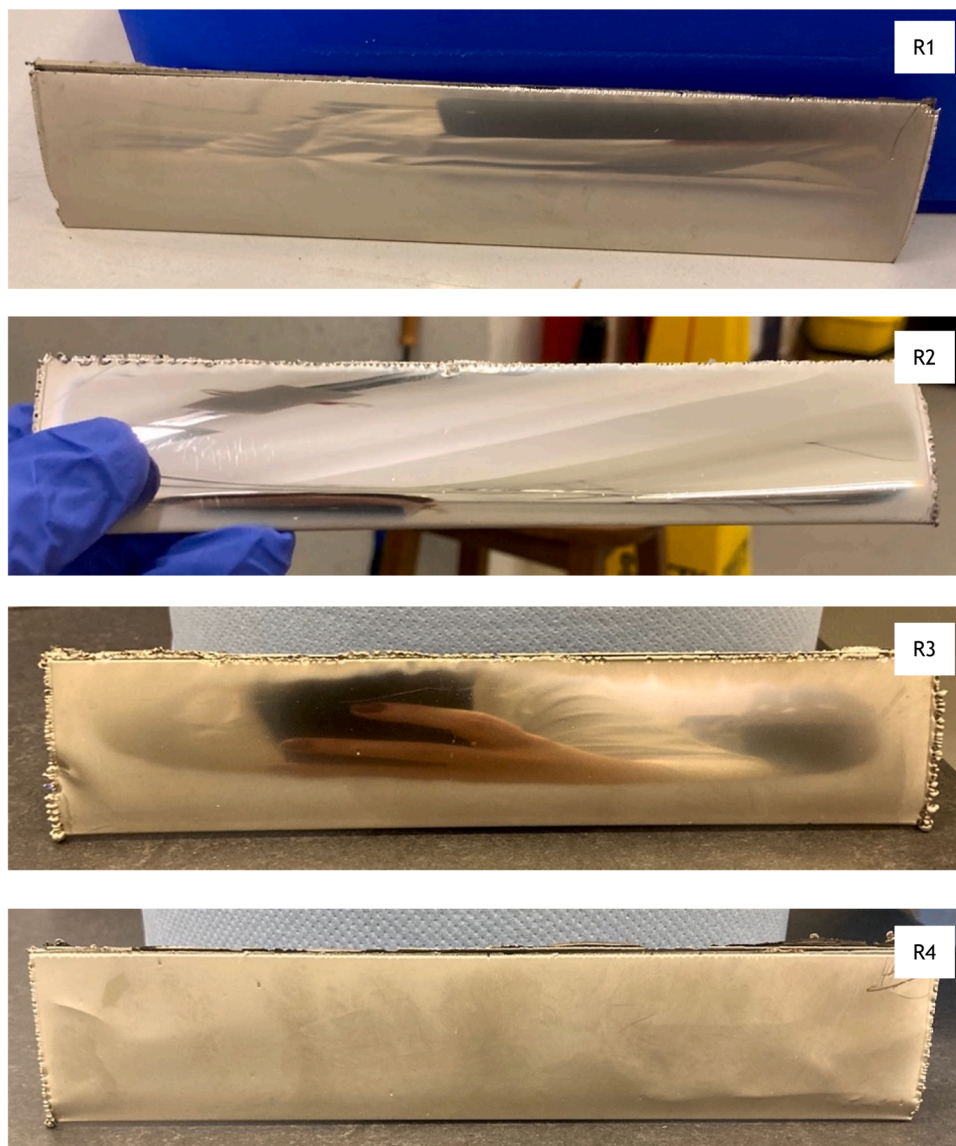
Fig. 10. Nickel mechanical vane electroforms R1, R2, R3 and R4. The gradual change in surface finishing is highlighted. Electroforms R1, R2 and R3 were produced at 1.11 A/dm^2, 2.44 A/dm^2 and 4.89 A/dm^2, respectively, after deposition for 5 h at 50 °C. Electroform R4 was produced at 4.89 A/dm^2 after deposition for 2.5 h at 50 °C.

Deposit R3 was sectioned across its width in three strips, as shown in Fig. 14a. One strip was retrieved from the middle of the part and two more on the left and right side of this middle section. The three strips were subsequently mounted in resin (Fig. 14b). The final specimen was placed under the optical microscope and studied at a × 20 magnification in terms of the sections' thickness. Measurements were taken at seven points (A-G) along each strip profile as indicated in Fig. 14b. The highest thickness was measured at the "nose" at an average of 0.63 mm. Table 5 summarises all the thickness measurements obtained for the specimen shown in Fig. 14b. Figures of all optical microscope thickness measurements are provided in Appendix I at the end of this chapter. The corresponding predicted thicknesses were retrieved from the modelling results along the three edges highlighted in orange in Fig. 14c.

Comparative plots of the experimental and simulated thickness profiles for each strip are provided in Fig. 15a & c. Fig. 16a & b provide, respectively, overlaps of the experimental and simulated thickness profiles of all three strips that the deposit R3 was sectioned to. Point A corresponds to a length section of 0.012 m while points D and G to 0.036 m and 0.061 m respectively. No thickness measurements were taken at the leading edges where dendrites formed. However, in all cases

higher thicknesses at the leading edges were simulated by the model as is highlighted by the green circles in Fig. 15.

As it can also be seen in Fig. 15, the model follows the experimentally observed thickness distribution with higher thicknesses simulated at the "nose" and lower ones at the front and side faces of the mandrel. Nevertheless, the model underpredicts the thickness at the "nose" area by almost 30%, while it is in reasonably good agreement with experimental thicknesses at the front and back faces of the tool.

Another interesting observation was that both experimental and modelling results in Fig. 16 show that the sides of the mandrel grow faster than its middle. Blue and red lines, corresponding to strips 1 and 3 retrieved from the sides of deposit R3, are perfectly overlap across the section length, while the orange line, corresponding to strip 2 retrieved from the middle of the deposit, lies consistently lower. This result is consistent with the qualitative observation that deposition is higher at the sides of the vane.

The agreement between the experimental and modelling results is not good, however, when it comes to the thicknesses of the front and back faces of the deposit. Reasonably, experimental results suggest that the front face, the one closer to the anode, grows faster than the back
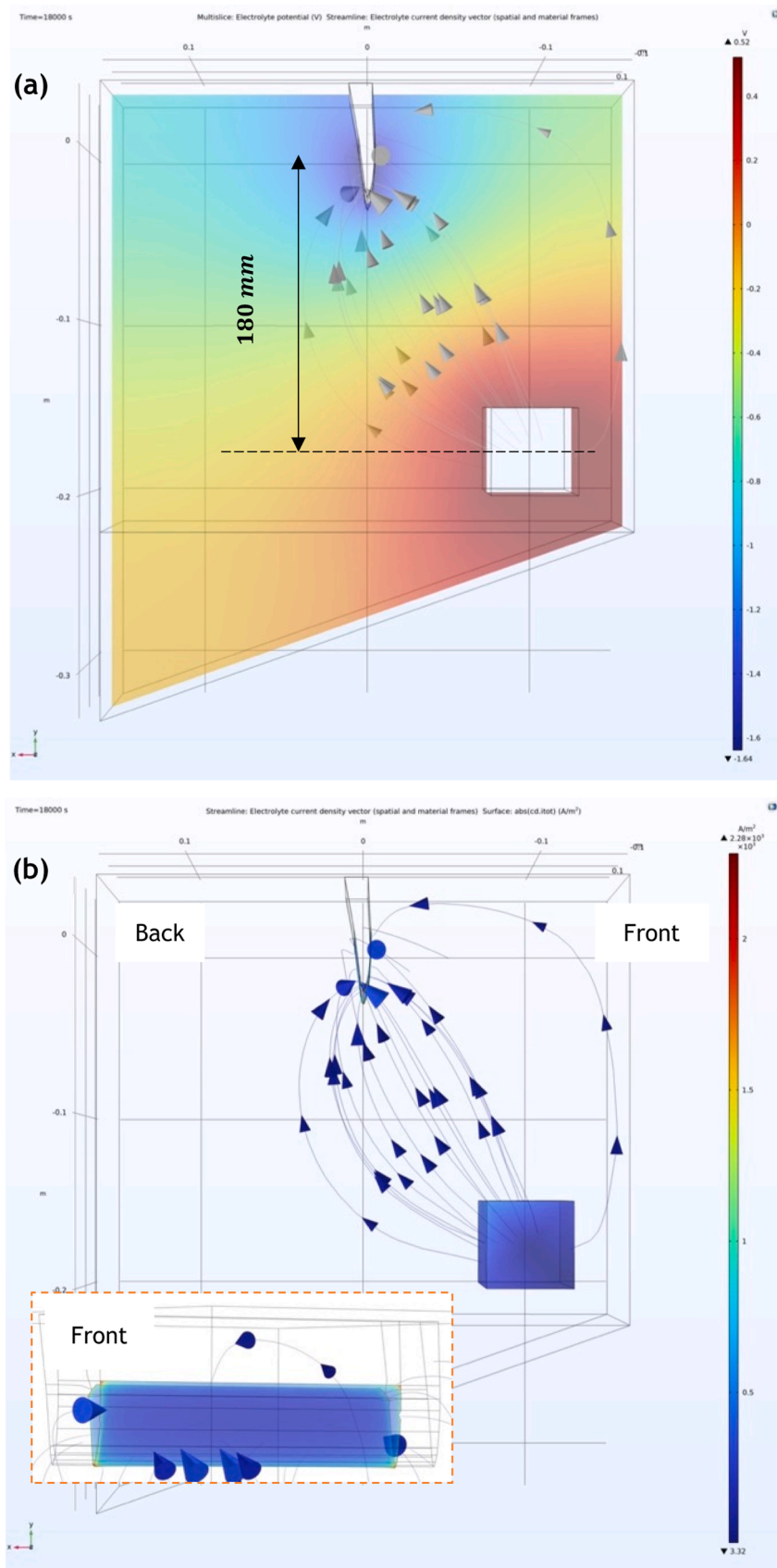
Fig. 11. 3-D representation of **(a)** the potential and **(b)** the current distribution in the electrolyte volume of the mechanical vane model. The results simulate potential and current distributions after 5 h at 50 °C. The vertical distance between the electrodes's geometrical centres is noted in figure **(a)**. Current distribution on the cathode surface is shown in the cathode surface close up provided in figure **(b)**.
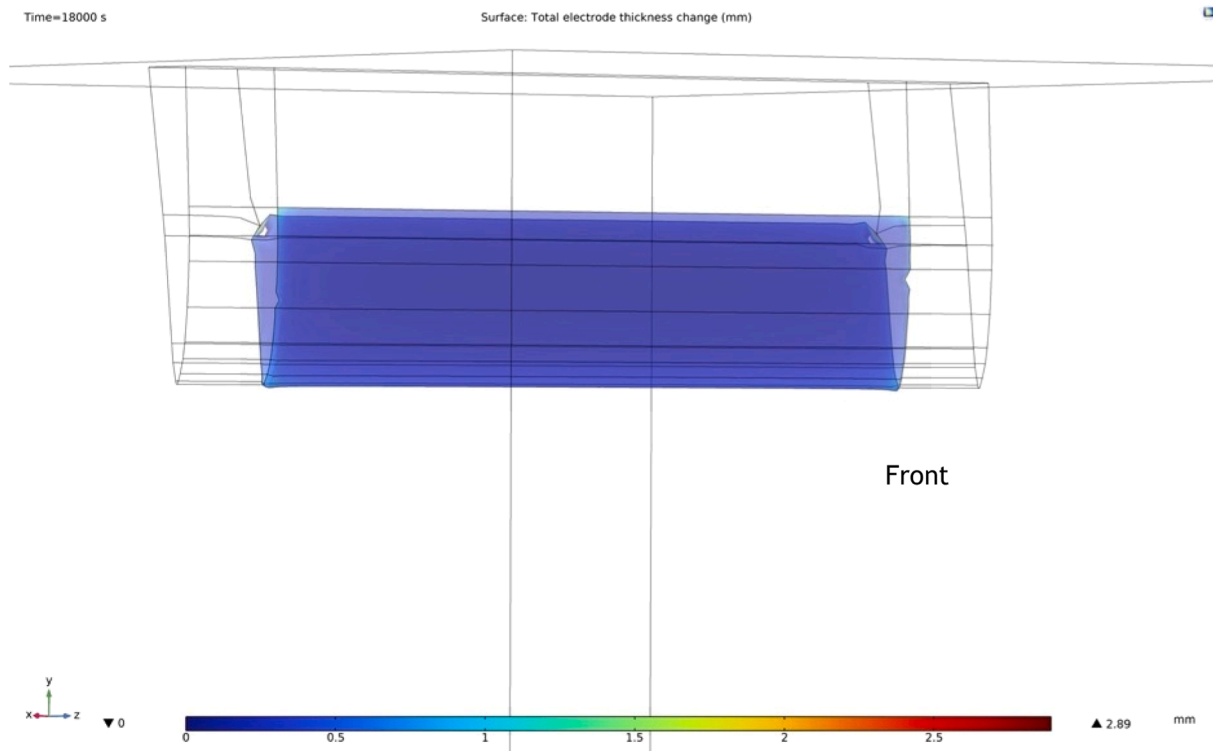
Fig. 12. Simulated deposit thickness distribution on the mechanical vane deposition area. Only the "front" face is shown. The simulated non-uniform thickness distribution follows the previously simulated non-uniform current distribution, with higher currents at the edges and lower at the centre.
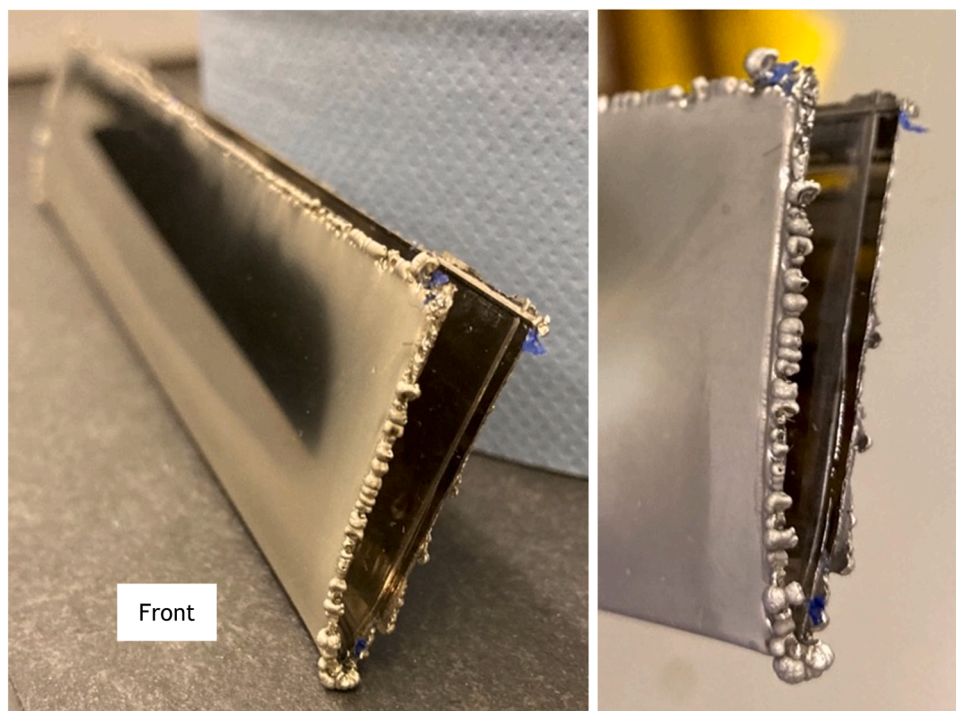

Fig. 13. Mechanical vane deposit R3. The deposit was formed of pure nickel and deposition was conducted at −5.4 V and − 4.4 A, for 18000 s, at 50 ˚C. "Front" indicates the mandrel side closer to the anode. The dendrites formed at the leading edges are also shown here.

face, resulting to higher thicknesses on the front face (Fig. 16a). This difference is not depicted in the modelling results which suggest no difference in the thickness (Fig. 16b).

On another note, target thicknesses (red lines) are provided in Fig. 15 for reference only; to achieve these thicknesses, someone should simply

apply higher currents for the same deposition duration, or just run the process for longer. Longer deposition hours were not possible within the working hours (8 h per day) of a university-based laboratory.

Higher currents were applied, though, resulting in thicker deposits, like electroform R6 shown in Fig. 9. For clarity, Fig. 17 shows the
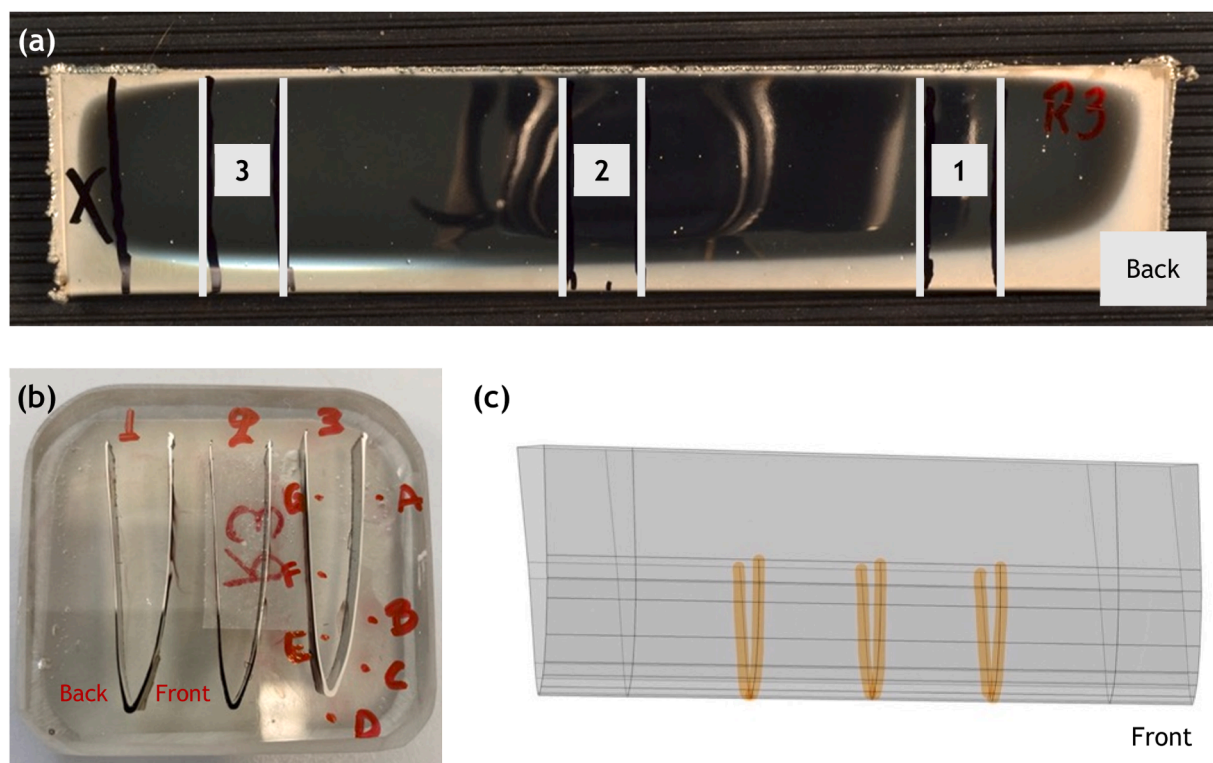
Fig. 14. (a) The three strips deposit R3 was sectioned in as seen from the "back" face of the mandrel. **(b)** Mandrel sections mounted in resin specimen. **(c)** Corresponding boundaries along which simulated thickness results were retrieved. Section length is measured from point I to points II and III shown in figure **(c)**.

Table 5
Deposit R3 thickness measurements collected under the optical microscope.

Deposit Strip	Deposit R3 Thickness (mm) 4.4 A (CC) − 5A/dm² − 5 h − 50°C						
1	**A**	**B**	**C**	**D***	**E**	**F**	**G**
	0.21	0.23	0.31	0.65	0.17	0.12	0.12
2	**A**	**B**	**C**	**D***	**E**	**F**	**G**
	0.2	0.2	0.27	0.59	0.19	0.11	0.1
3	**A**	**B**	**C**	**D***	**E**	**F**	**G**
	0.21	0.23	0.3	0.66	0.19	0.13	0.12

* Average of three measurements at the "nose".

experimental and simulated thickness profiles for the corresponding strips 1, 2 and 3 of electroform R6. As it can be seen here, deposition at 7.22 A/dm² for 5 h results in thicknesses within the target values towards the tool's sides, while even at the middle of the mandrel, where deposition progresses slower, thicknesses touch the minimum target thickness values. Nevertheless, Fig. 17 also demonstrates that the model underpredicts the thickness values. In that instance, the model underpredicts both the thicknesses at the "nose" area (by almost 40 %) as well as those at the front and back faces of the mandrel (by almost 20 %). Subsequently, the conclusion is drawn that the deviation between the experimental and simulation results increases with the increase of the applied current density value.

Even though the mechanical vane model might be necessary to undergo further optimisation studies in order to improve the agreement with the experiments, in terms of the numerical results, it is proposed here that it can confidently be used for qualitative studies as is. Although the mechanical vane model underpredicts the thicknesses to be achieved at higher current densities, it, at least, confirms that vane electroforms can be successfully produced. For deposition at current densities up to ∼ 5 A/dm² simulated thicknesses can even be quantitatively, and not only qualitatively, validated by experiments. Since our industrial partners produce the mechanical vane electroforms at ∼ 2 A/dm², the model is

proposed to fit the purposes of this specific process.

4.3. Deposit structural characterisation

Even though structural characterisation of the electroforms was not one of the direct objectives of this project, it was believed that an analysis of that kind, at a preliminary level, would allow for a complete qualitative validation of the experimental studies, allowing to confirm the material growth mechanism, grain size and composition of the electroforms. Scanning electron microscopy (SEM) was used for this purpose (Vernon-Parry, 2000). Compositional analysis of the samples under investigation was also conducted using the back-scattered electrons (BSE) beam of the SEM.

For the SEM measurements presented here, a *Hitachi S3700-N Scanning Electron Microscope* was used, located at the *Advanced Materials Research Laboratory* (AMRL) at the University of Strathclyde.

The microscope is equipped with both secondary electrons and back-scattered electrons detectors. Emission of secondary electrons was used for surface analysis while back-scattered ones were used for compositional analysis of the samples, alongside energy dispersive spectroscopy (EDS) for detailed elemental analysis. Analysis was run under a 10 kV emission field.

Fig. 18 was produced by SEM imaging of the strip 2 section surface of the etched R3 electroform, at magnification × 3, 000, using the secondary electrons beam. The resin specimen, including the three electroform strips, as shown in Fig. 14b, was gold-coated before introduced in the SEM chamber for analysis and fixed on the SEM holder by copper tape. This allowed for the resin specimen to be conductive and allow for the electrons to interact with the metallic samples, *i.e.*, the three electroform strips. The specimen was etched by being immersed in a solution of 50% nitric and 50% acetic acid for 5 s. Even though various etching solutions and immersion times were used, all etched specimens obtained did not exhibit sufficient microstructural detail for analysis. However, for the purposes of this work, the quality of etching shown in Fig. 18 was
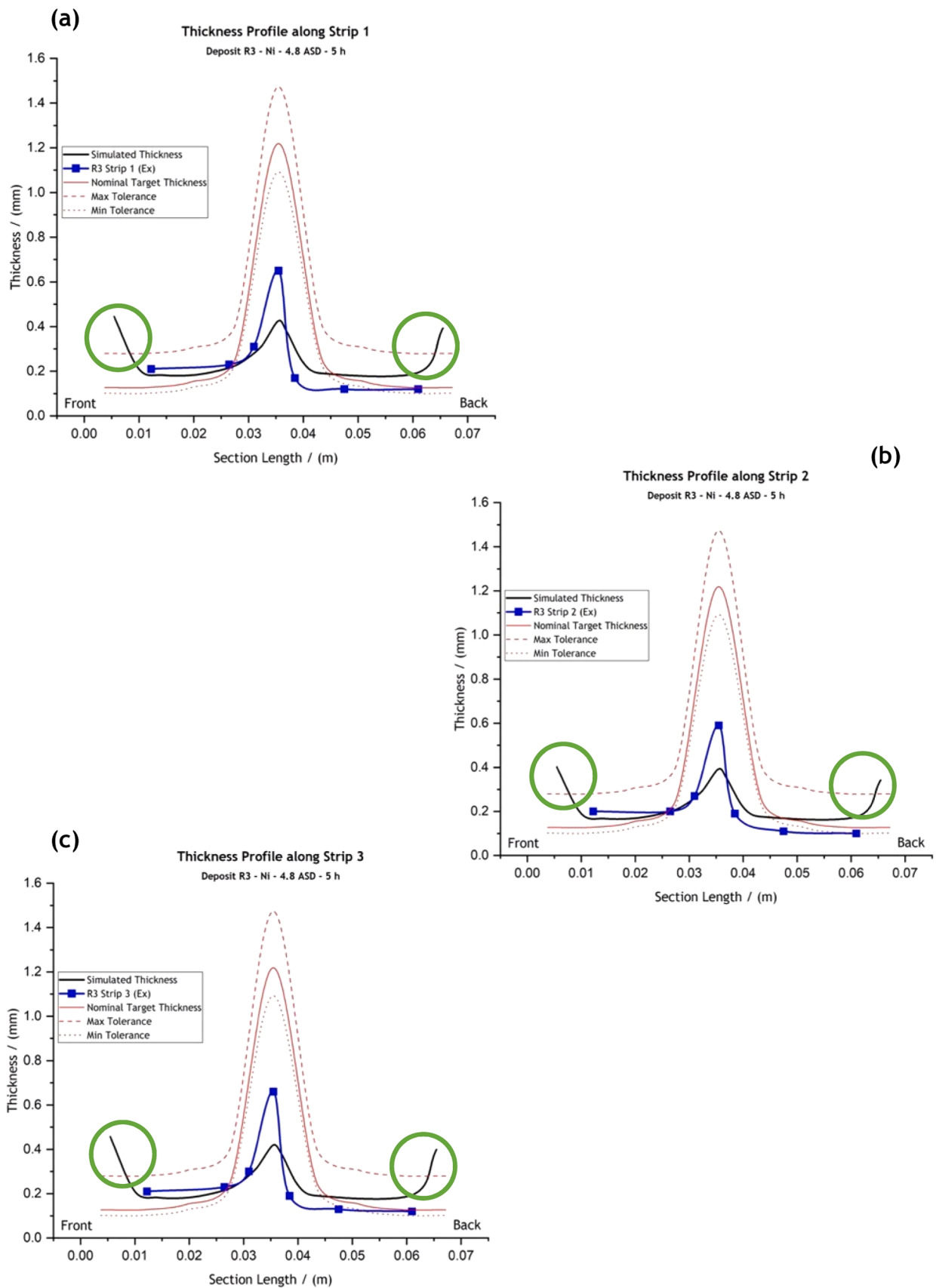
Fig. 15. Comparative graphs of the experimental and simulated thickness profiles for **(a)** strip 1, **(b)** strip 2 and **(c)** strip 3 of the mechanical vane deposit R3. Deposition of R3 was conducted at −5.4 V and − 4.4 A, for 18000 s, at 50 °C. "Front" indicates the mandrel side closer to the anode. Circles highlight thicknesses that correspond to dendritic growth.
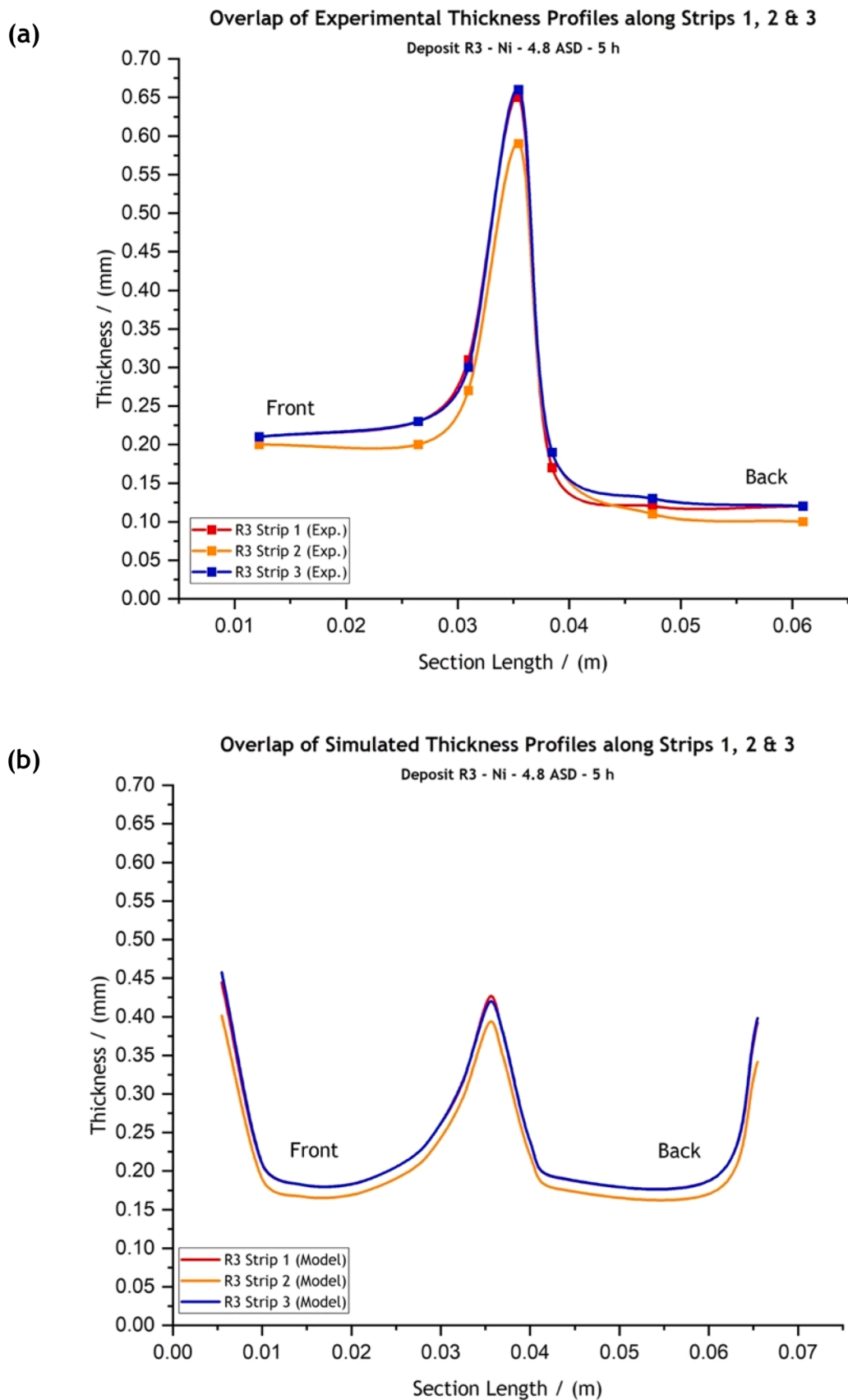
(a)

(b)

Fig. 16. Overlaps of **(a)** the experimental and **(b)** the simulated thickness profiles for strips 1, 2 and 3 of the mechanical vane deposit R3. Deposition of R3 was conducted at −5.4 V and − 4.4 A, for 18000 s, at 50 °C. "Front" indicates the mandrel side closer to the anode.

Fig. 17. Comparative graphs of the experimental and simulated thickness profiles for **(a)** strip 1, **(b)** strip 2 and **(c)** strip 3 of the mechanical vane deposit R6. Deposition of R6 was conducted at −6.5 V and − 6.5 A, for 18000 s, at 50 °C. "Front" indicates the mandrel side closer to the anode.
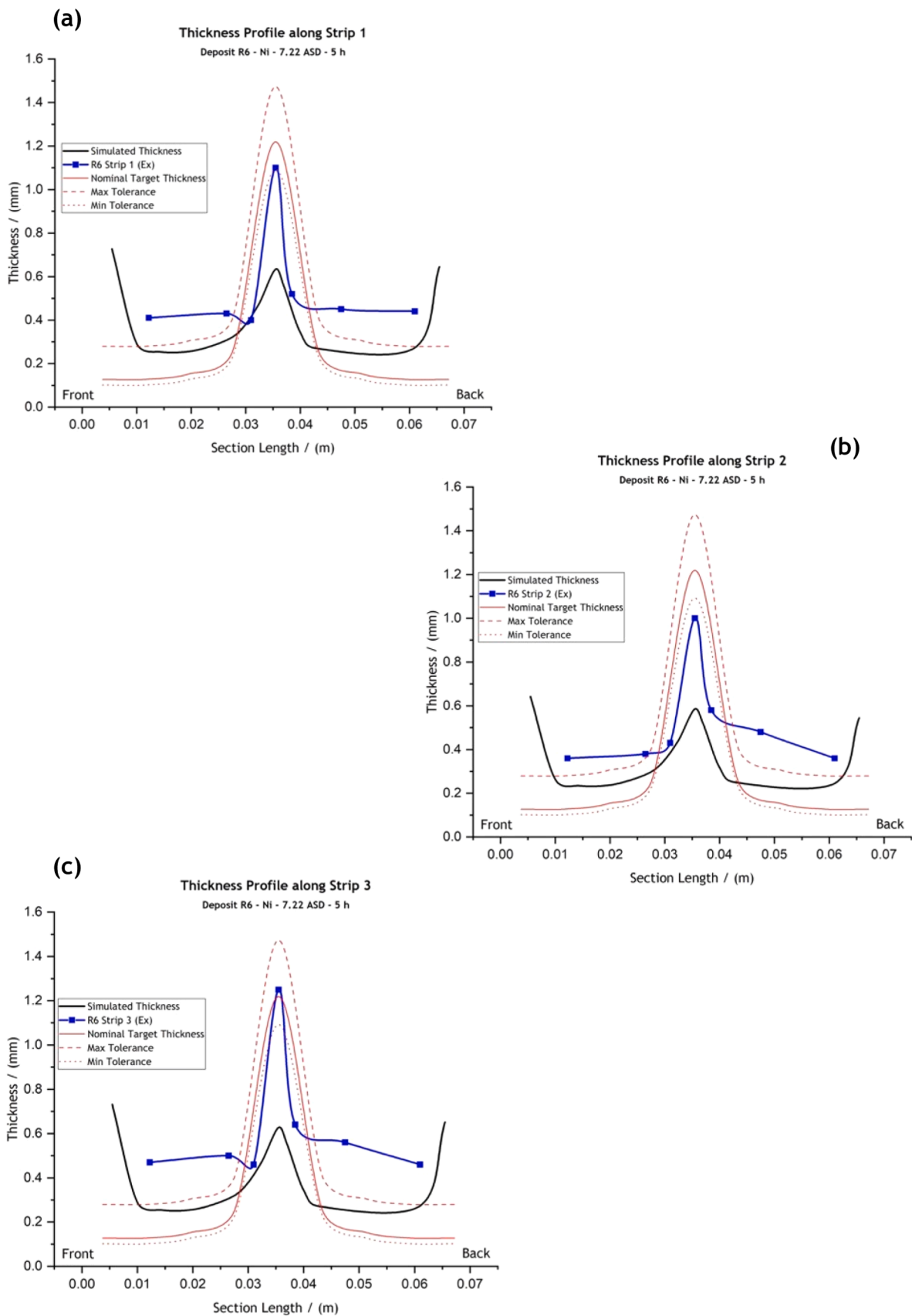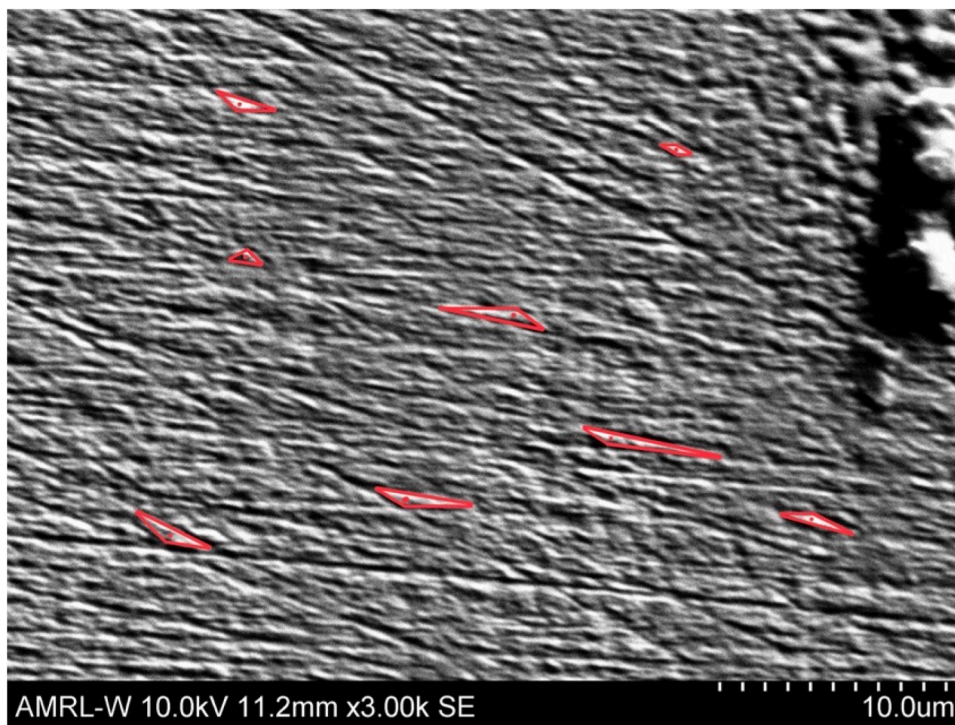
Fig. 18. Scanning electron microscopy imaging of the strip 2 section surface of the etched R3 electroform at magnification $\times$ 3,000. The red triangles indicate the boundaries of what believed to be pyramid-shaped nickel grains evolving during deposition. The red dots within the red triangles indicate the "tip" point of the pyramid-shaped grains indicating growth on the z-direction (outwards from the page level).
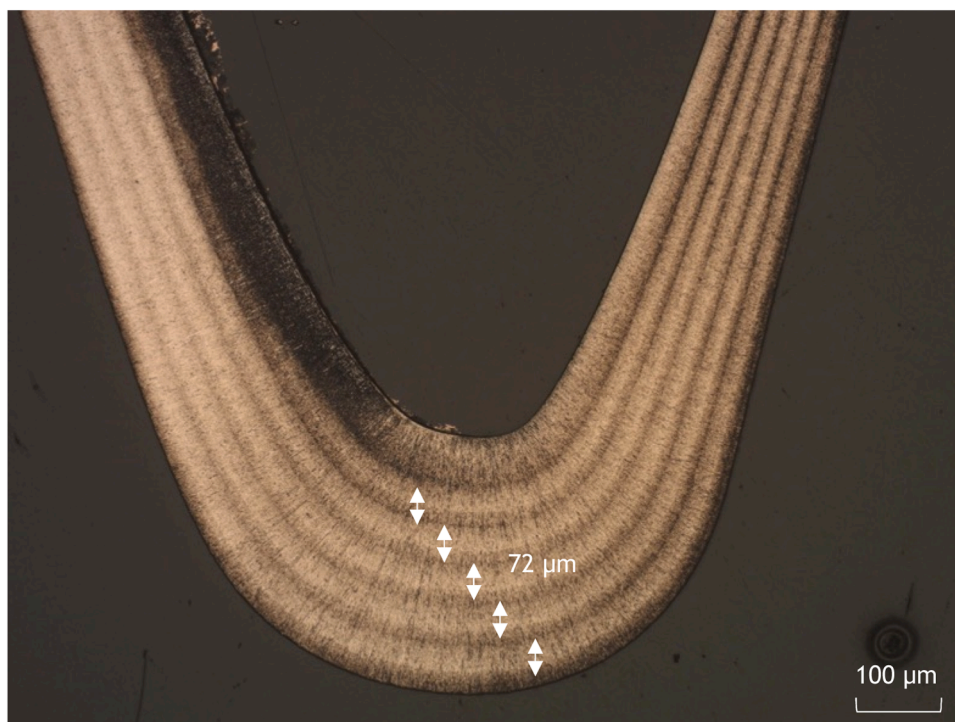

Fig. 19. Electronic microscope imaging of the strip 2 "nose" section surface of the etched R3 electroform at magnification $\times$ 50. The growth mechanism presents a periodicity which leads to "necklace"-like zones of $\sim$ 72 μm in thickness.

considered to be sufficient.

Analysis of Fig. 18 suggested that pyramid-shaped nickel particles are developing and growing layer by layer in a lamellar fashion. The red triangles indicate the boundaries of what believed to be pyramid-shaped nickel grains evolving during deposition. The red dots within the red triangles indicate the "tip" point of the pyramid-shaped grains indicating lamellar growth outwards from the page level. This particle evolution mechanism has also been reported in other works (Mahapatra,
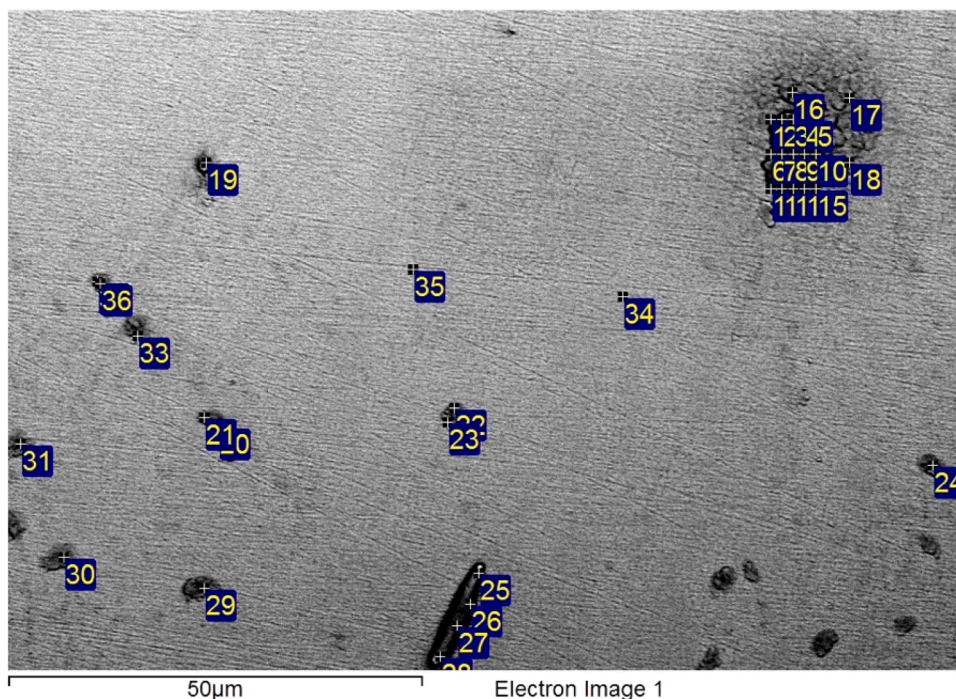
Fig. 20. Spots of elemental analysis under the scanning electron microscope using the backscattered-electron beam alongside energy dispersive spectroscopy.

Table 6
EDS elemental analysis of the etched R3 electroform.

Spectrum	Ni	O	N	Si	Cl	Ca	Total
1	83.04	12.58		1.30		3.08	**100.00**
2	87.37	12.63					**100.00**
3	94.37	5.63					**100.00**
4	94.34	5.66					**100.00**
5	91.88	8.12					**100.00**
6	92.77	7.23					**100.00**
7	89.54	10.46					**100.00**
8	90.29	9.71					**100.00**
9	94.32	5.68					**100.00**
10	78.63	18.84	2.53				**100.00**
11	93.72	6.28					**100.00**
12	92.84	7.16					**100.00**
13	94.16	5.84					**100.00**
14	62.11	26.32		3.24		8.33	**100.00**
15	64.19	34.49			1.33		**100.00**
16	97.11	2.89					**100.00**
17	95.63	4.37					**100.00**
18	73.99	22.80	3.21				**100.00**
19	98.76	1.24					**100.00**
20	99.01	0.99					**100.00**
21	100.00						**100.00**
22	99.11	0.89					**100.00**
23	99.17	0.83					**100.00**
24	98.95	1.05					**100.00**
25	99.14	0.86					**100.00**
26	99.09	0.91					**100.00**
27	98.96	1.04					**100.00**
28	99.15	0.85					**100.00**
29	98.92	1.08					**100.00**
30	98.99	1.01					**100.00**
31	98.99	1.01					**100.00**
32	98.95	1.05					**100.00**
33	99.16	0.84					**100.00**
34	98.80	1.20					**100.00**
35	100.00						**100.00**
36	98.91	1.09					**100.00**

2020, Wanga et al., 2006).

In an effort to provide an explanation for lamellar growth of various metal electrodeposits, Winand (1991, 1994) suggested that lamellar growth is one of the several types of deposit growth mechanisms which occur due to the competition among crystals that grow vertically and crystals that grow laterally. This competition takes place since lateral crystal growth will at some point be stopped either due to a decrease of the local current density or simply because a neighbouring crystal will get on the way. Specifically for nickel, Delplancke et al. (1993) reported lamellar growth in $Ni - P$ foils while, Tian et al. (2020) successfully developed a lamellar $Ni - W - Graphene\ Oxide$ coating. The latter suggested that lamellar growth is driven by an increase in current (up to $12\ \mathrm{A/dm^2}$) which enhances nucleation and inhibits grain growth by graphene oxide sheets. Additionally, they also suggested that lamellar growth is a result of the alternating growth of lateral and vertical crystals. Importantly, it is this lamellar growth that is proposed to enhance the deposits' corrosion resistance due to the high corrosion potential and low corrosion current (Tian et al., 2020; Goldstein, 2003).

SEM characterisation led to another interesting structure-related observation. As it can be seen in Fig. 19, at magnification $\times$ 50 under the electronic microscope of the etched R3 electroform, the growth mechanism presents a periodicity which leads to "necklace"-like zones of $\sim$ 100 μm in thickness at the "nose". This observation is an important one since, to the authors' best knowledge, it has not been reported before. Even though this seems to be a material behaviour worth investigating further in the future, the working theory in the context of this project is that these periodic layers coincide with a periodic re-nucleation of the active $NiOH_{ads}$ intermediate, formed during the rate-determining step of the nickel deposition mechanism proposed in a previous publication (Roy and Andreou, 2020) and described by the chemical reaction (1) below:

$$Ni(OH)^+ +\ e^- \rightleftharpoons Ni(OH)_{ads} \tag{1}$$

In the authors' opinion, further investigations of this behaviour are of essence to determine whether this periodic layer formation coincides with a periodic transition between different crystallographic phases, or re-nucleation, possibly also affecting the internal stresses developing in
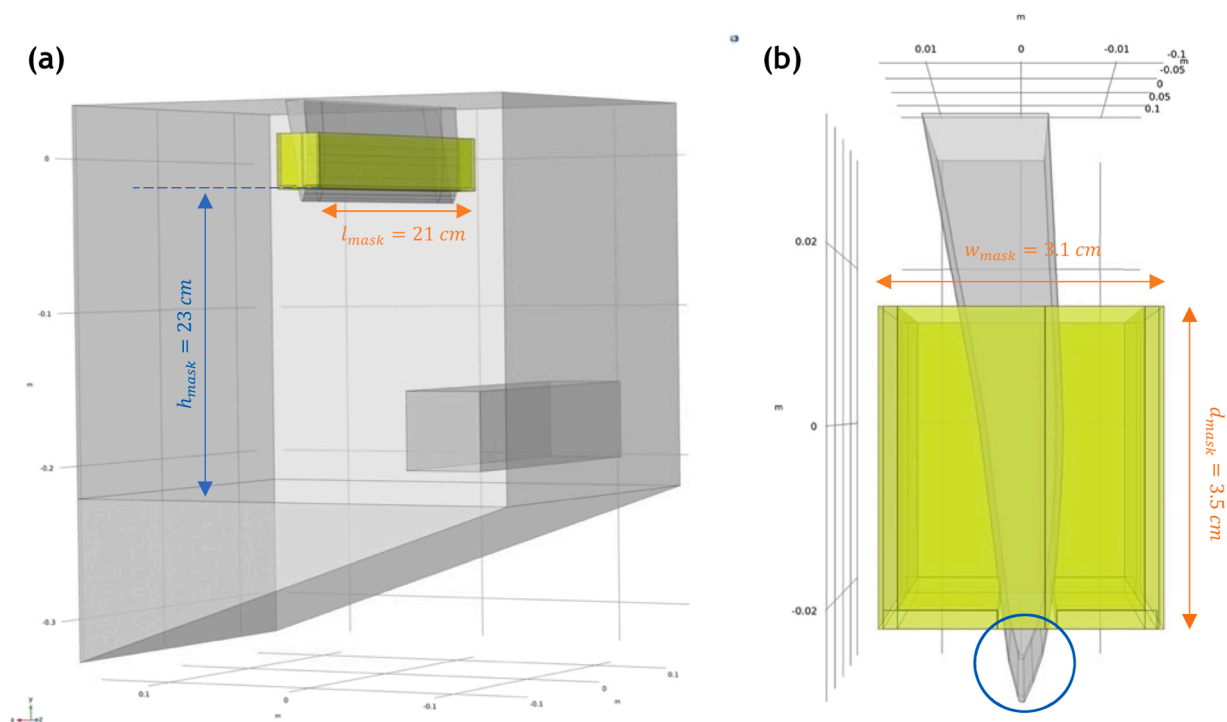
(a)

(b)

Fig. 21. **(a)** 3-D geometry of the mechanical vane setup including a "shell"-type "mask" at $h_{mask} = 23$ cm from the flat bottom of the prototype tank. **(b)** Side view of the "shell"-type "mask". The dimensions of the "mask" are also shown. The circle indicates the "nose" area of the mandrel.

the final products, either in a positive or a negative way.

Following the analysis presented so far, the backscattered-electron beam was used for compositional analysis of the sample, alongside energy dispersive spectroscopy (EDS) for detailed elemental analysis. The spots of analysis are shown in Fig. 20 and the elemental analysis is provided in Table 6.

As it is evident, elemental analysis suggests that the electroform consists, predominantly, of pure nickel. The only other element consistently present in the sample was found to be oxygen at low levels throughout the deposit, mostly at 1% or less. This might be an additional indication supporting the working theory that the active $NiOH_{ads}$ intermediate, which is periodically re-nucleating throughout the process, is also the source of the oxygen measured in the sample. The other elements (N, Si, Cl, Ca) occasionally measured as part of the sample's composition are included in the resin composition and, as such, could be considered random occurrences in which case should be ignored. However, one notices that the corresponding oxygen content at these locations is also high. It is possible that there the surfactant may have been "included" in the deposit, which would explain the presence of other elements and oxygen.

4.4. "Masks" alongside the mechanical vane mandrel

As it has already been mentioned, the thickness requirements for the mechanical vane geometry call for deposits thicker at the "nose" area and considerably thinner at the sides. Based on the experimental results presented in Fig. 17 for deposit R6, if the process parameters are set so that they accommodate higher thicknesses at the "nose" (*e.g.*, higher applied currents, longer deposition times) then the sides will overgrow even the acceptable maximum thickness tolerance. This behaviour constitutes a really good example of a case when the use of "masks" should be considered in industry for process optimisation purposes.

In Fig. 21 a "shell"-type "mask" is shown, essentially being a box with a slit at its bottom side to allow for the "nose" area to get through it (Fig. 21b), and without a top side. The "mask" was positioned around the cathode at $h_{mask} = 23$ cm from the flat bottom of the tank (Fig. 21a).

The masking box was of a length $l_{mask} = 21$ cm (Fig. 21a), width $w_{mask} = 3.1$ cm and depth $d_{mask} = 3.5$ cm (Fig. 21b).

The idea was to "protect" most of the vane mandrel surface from all sides, allowing the current to reach it from the exposed area "from the top" of the "mask", as indicated in Fig. 22a & b by the orange arrows resulting in thinner deposits there compared to the "nose" area of the mandrel. The "nose" was the only mandrel area left exposed by the "mask", with the current reaching it directly. This arrangement would result in higher current accumulation around the "nose" area (Fig. 22b) and, consequently, higher thicknesses there (Fig. 22c).

As Fig. 23 indicates, the simulations suggested that the deployment of the "shell"-type "mask" alongside the mechanical vane mandrel would prevent overgrowth at the sides of the mandrel and increase the thickness of the "nose", bringing the overall thickness distribution across the mandrel's surface closer to the target thickness profile. Specifically, the green profiles in Fig. 23 indicate that the mandrel's back and front sides will grow slower, while the "nose" will grow faster, compared to what is the case when no "mask" is deployed (indicated by the blue thickness profiles). This means that, in practice, the process could be run for slightly longer than 5 h (resulting in deposit R6, black thickness profile), in order to eventually allow the "nose" to reach its target thickness while the front and back side thicknesses are also kept within the lower acceptable thickness targets.

As a note, one should keep in mind that these modelling results have not been confirmed by practical experiments therefore, they should be accepted cautiously. However, the fact that the modelling results confirm the working theory that a "shell"-type "mask's" function could be is of great importance. Carrying out such simulations shows the value of a well-informed modelling tool which allows manufacturers to virtually investigate potential optimisation routes before deciding to invest time, money, materials, and energy to the manufacturing process of a part.

5. Conclusions

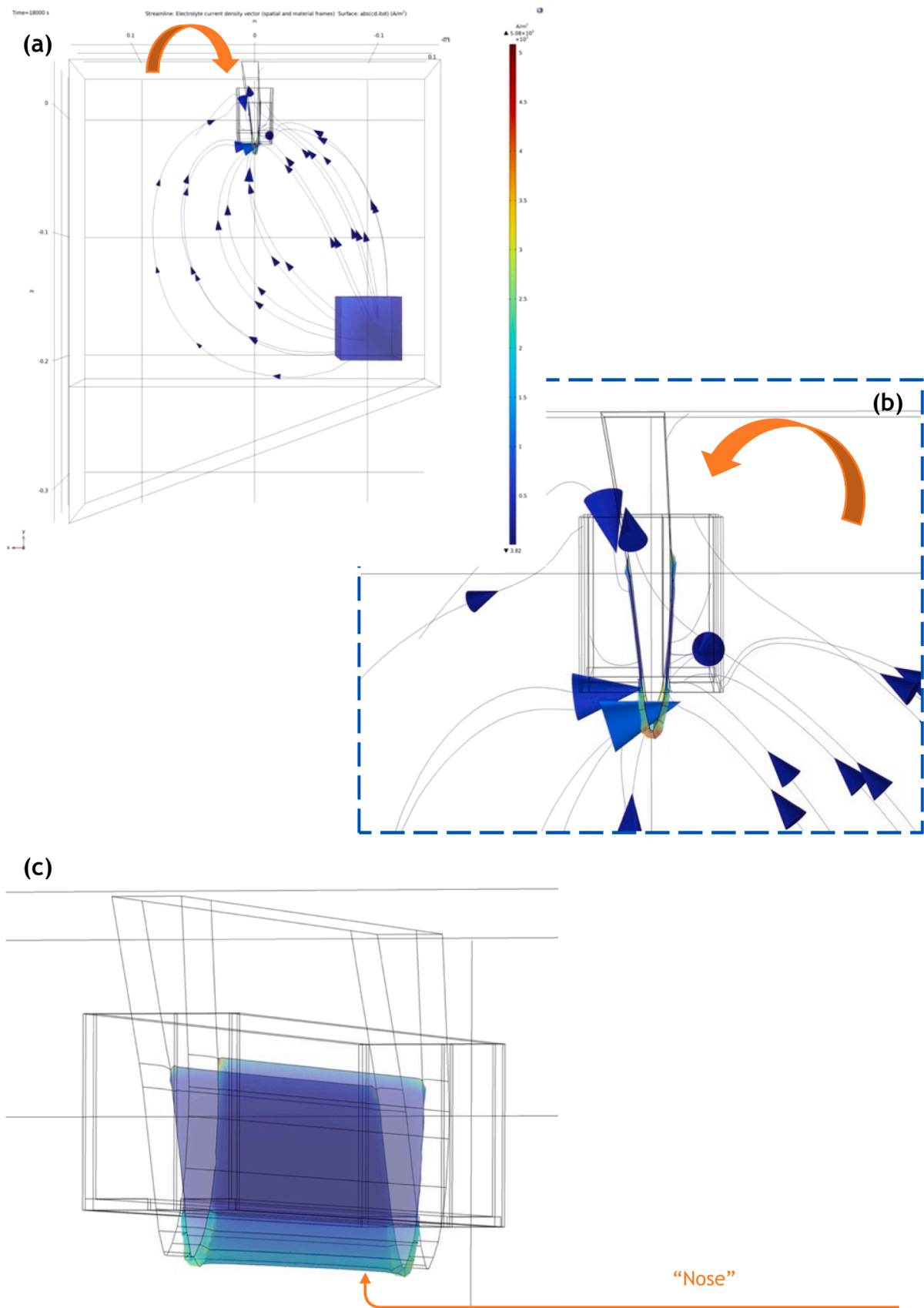Nickel deposits were formed to validate a 3-D, time-dependent,

Fig. 22. (a) 3-D representation of the current distribution in the electrolytic volume, **(b)** current streamlines' behaviour close to the mandrel surface and **(c)** thickness distribution on the cathode surface for the case when the a "shell"-type "mask" is used alongside the mechanical vane mandrel. The arrows in **(a)** and **(b)** indicates the current reaching the mandrel sides indirectly "from the top" while, **(c)** indicates the exposed "nose" area of the mandrel which the current reaches directly.
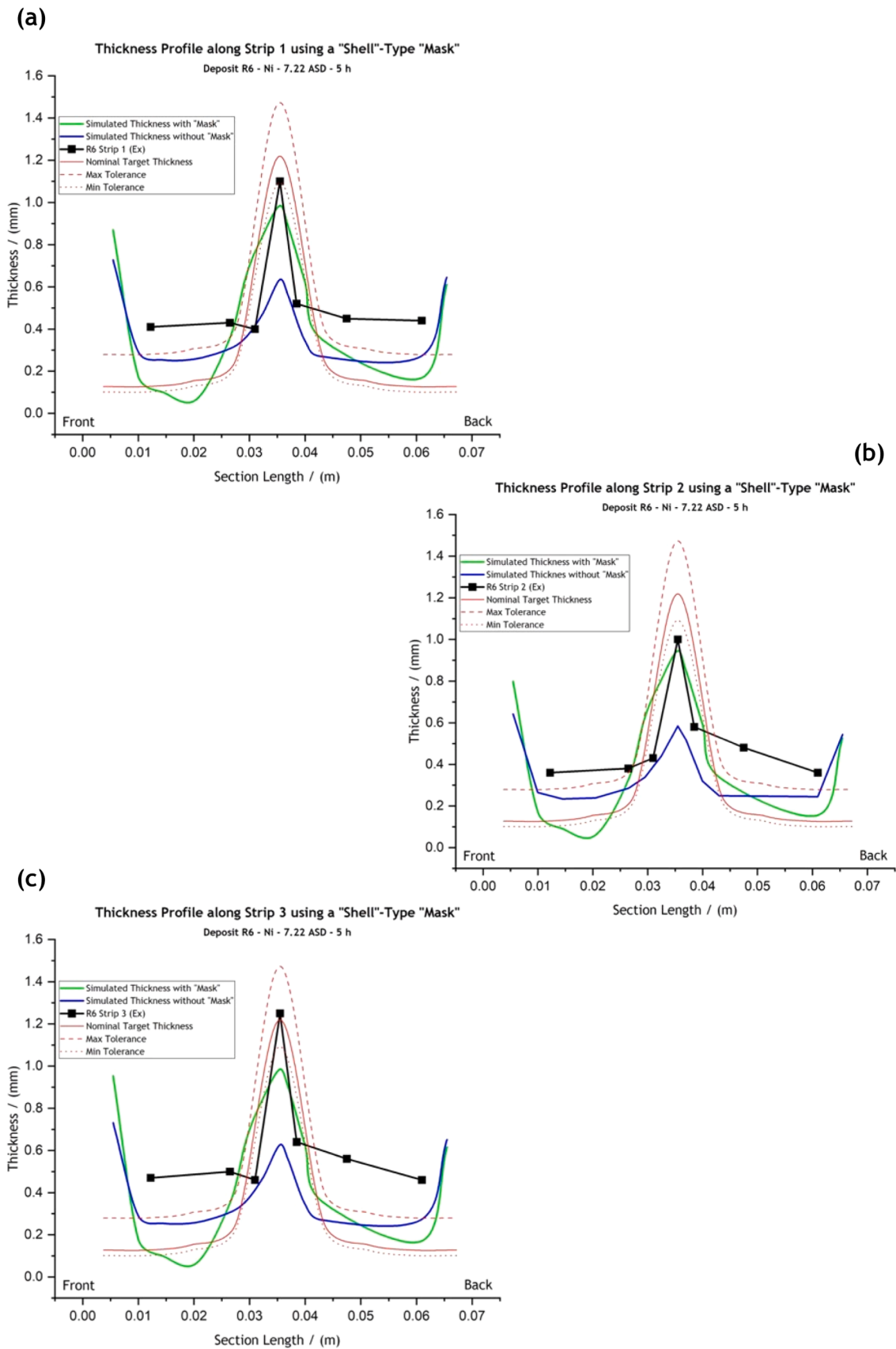
(a)

(b)

(c)

Fig. 23. Comparative graphs of the experimental and simulated thickness profiles for **(a)** strip 1, **(b)** strip 2 and **(c)** strip 3 of the mechanical vane deposit R6. Green line represents the simulated thickness for R6 alongside a "shell"-type "mask", while the blue line represents the simulated thickness for R6 without the use of a "mask". "Front" indicates the mandrel side closer to the anode.

secondary distribution model of a mechanical vane electroforming process. The mandrel presents industrial interest as the final parts are used for demanding aerospace applications.

Experimental results revealed that deposition progresses from the sides of the cathode towards its centre, with a faster deposition rate at the sides of the mandrel compared to that in the middle. The process was confirmed to be predictable, with the deposited nickel mass presenting an analogous relationship with both the applied current density and deposition time. Additionally, deposition experiments revealed a correlation between the applied current density and the electroforms' surface finishing, with higher current densities or longer periods of deposition resulting in a matte surface finishing.

The modelling studies at current densities up to 5 A /dm^2 predicted the experimentally observed thickness distribution, with higher thicknesses simulated at the "nose" and lower ones at the front and side faces of the mandrel. On the other hand, simulations at current densities higher than 5 A/dm^2 underpredicted both the thicknesses at the "nose" area (by almost 40 %) and those at the front and back faces of the part (by almost 20 %). Consequently, it is proposed that the model can confidently be used for quantitative studies of a mechanical vane electroforming process at current densities up to 5 A/dm^2, but only for qualitative studies at higher ones.

Scanning electron microscopy suggested that pyramid-shaped nickel particles evolve during deposition. For the first time, periodic "necklace"-like zones of $\sim 100~\mu$m in thickness at the "nose" area are also reported, potentially coinciding with a periodic re-nucleation of the active $NiOH_{ads}$ intermediate. Further structural characterisation is proposed to investigate the possibility that this periodic layer formation also coincides with a periodic transition between different crystallographic phases, possibly affecting the internal stresses of the final products.

Lastly, a qualitative assessment of the model's ability to simulate the effect of "masks" on the electroforming process was carried out. Even though experimental validation of the relevant modelling results is required, the simulations strongly indicated that "masks" could potentially be an important aid in the efforts to decrease dendritic growth at mandrel leading edges just through modifications of the process setup's geometry.

CRediT authorship contribution statement

Eleni Andreou: Writing – original draft, Visualization, Validation, Software, Methodology, Investigation, Formal analysis, Data curation. **Sudipta Roy:** Writing – review & editing, Supervision, Resources, Project administration, Funding acquisition, Conceptualization.

Declaration of competing interest

The authors declare the following financial interests/personal relationships which may be considered as potential competing interests:

Eleni Andreou reports financial support was provided by Scottish Research Partnership in Engineering (SRPe). Eleni Andreou reports financial support, equipment, drugs, or supplies, and travel were provided by Radius Aerospace Bramah. If there are other authors, they declare that they have no known competing financial interests or personal relationships that could have appeared to influence the work reported in this paper.

Data availability

Data will be made available on request.

Supplementary materials

Supplementary material associated with this article can be found, in the online version, at doi:10.1016/j.dche.2024.100177.

References

Alkire, R., Bergh, T., Sani, T., 1978. Predicting electrode shape change with use of finite element methods. J. Electrochem. Soc. 125, 1981.

Andreou, E., Roy, S., 2021. Modelling the electroforming process: significance and challenges. Trans. IMF 99 (6), 299–305.

Andreou, E., Roy, S., 2022. Modelling the scaling-up of the nickel electroforming process. Front. Chem. Eng. 4, 755725.

Berman, B., 2012. 3-D printing: the new industrial revolution. Bus. Horiz. 55, 155–162.

Blanqui, J.-A. History of political economy in Europe, E. J. Leonard, Ed., New York: Putnam, 1880.

Chen, D., Heyer, S., Ibbotson, S., Salonitis, K., Steingrimsson, J., Thiede, S., 2015. Direct digital manufacturing: definition, evolution, and sustainability implications. J. Clean. Prod. 107, 615–625.

Delplancke, J., Winand, R., Dierickx, M., Lifschitz, L., 1993. Influence of low phosphorus concentration on the Electrocrystallization and the properties of Ni-P foils. J. Electrochem. Soc. 140, 2800.

Ford, S., Despeisse, M., 2016. Additive manufacturing and sustainability: an exploratory study of the advantages and challenges. J. Clean. Prod. 137, 1573–1587.

Goel, T., Dorney, D.J., Haftka, R.T., Shyy, W., 2008. Improving the hydrodynamic performance of diffuser vanes via shape optimization. Comput. Fluids. 37, 705–723.

Goldstein, J., 2003. Scanning Electron Microscopy and X-Ray Microanalysis. Springer, US.

Green, T.A., Tambe, C.E., Roy, S., 2022. Characteristics of anode materials for nickel electroforming. J. Electrochem. Soc. 169, 092510.

Heydari, H., Ahmadipouya, S., Maddah, A.S., Rokhforouz, M.-R., 2020. Experimental and mathematical analysis of electroformed rotating cone electrode. Korean J. Chem. Eng. 37 (4), 724–729.

Hogner, L., Nasuf, A., Voigt, P., Voigt, M., Vogeler, K., Meyer, M., Berridge, C., Goenaga, F., 2016. Analysis of high pressure turbine nozzle guide vanes considering geometric variations. In: ASME Turbo Expo2016: Turbomachinery Technical Conference. Seoul.

Huang, S., Liu, P., Mokasdar, A., Hou, L., 2013. Additive manufacturing and its societal impact: a literature review. Int. J. Adv. Manuf. Technol. 67, 1191–1203.

Madhwesh, N., Karanth, K.V., Sharma, N.Y., 2011. Impeller treatment for a centrifugal fan using splitter vanes - a CFD approach. In: World Congress on Engineering. London.

Mahapatra, M.K., 2020. Microstructure of electrodeposited nickel: role of additives. J. Mater. Eng. Perform. 29 (11), 7555–7566.

Masuku, E., Mileham, A., Hardisty, H., Bramley, A., Johal, C., Detassis, P., 2002. A finite element simulation of the electroplating process. CIRP Ann. 51 (1), 169–172.

Müller, J., Buliga, O., Voigt, K., 2018. Fortune favors the prepared: how SMEs approach business model innovations in Industry 4.0. Technol. Forecast. Soc. Change 132, 2–17.

Oh, Y., Chung, S., Lee, M., 2004. Optimisation of thicknes uniformity in electrodeposition onto a patterned substrate. Mater. Trans. 45 (10), 3005–3010.

Parkinson, R., 1998. Electroforming-A Unique Metal Fabrication Process. Nickel Development Institute, London, UK.

Petrick, I., Simpson, T., 2013. 3D Printing disrupts manufacturing: how economies of one create new rules of competition. Res.-Technol. Manage. 56 (6), 12–16.

Petrovic, V., Gonzalez, J., Ferrando, O., Gordillo, J., Puchades, J., Grinan, L., 2011. Additive layered manufacturing: sectors of industrial application shown through case studies. Int. J. Prod. Res. 49 (4), 1061–1079.

Popkova, E.G., Ragulina, Y.V., Bogoviz, A.V., 2019. Industry 4.0: Industrial Revolution of the 21st Century (Studies in Systems, Decision and Control), 169. Springer International Publishing AG.

Rolls-Royce, 1986. The Jet Engine, 5th ed. Rolls-Royce, Derby.

Roy, S., Andreou, E., 2020. Electroforming in the Industry 4.0 Era. Curr. Opin. Electrochem. 20, 108–115.

Slusarczyk, B., 2018. Industry 4.0: are we ready? Polish J. Manage. Stud. 17 (1), 232–248.

Tian, S., Gao, K., Zhang, H., Cui, H., Zhang, G., 2020. Corrosion resistance and anti-wear properties: Ni–W–GO nanocomposite coating with lamellar structure. Trans. Indian Inst. Metals 73 (3), 713–724.

Todd, J.T., Norman, J.F., 2018. The visual perception of metal. J. Vis. 18 (3), 1–17.

Uriondo, A., Esperon-Miguez, M., Perinpanayagam, S., 2015. The present and future of additive manufacturing in the aerospace sector: a review of important aspects. J. Aerosp. Eng. 229 (11), 2132–2147.

Vaidya, S., Ambad, P., Abhosle, S., 2018. Industry 4.0 - a glimpse. Procedia Manuf. 20, 233–238.

Vernon-Parry, K.D., 2000. Scanning electron microscopy: an introduction. III-Vs Rev. 13 (4), 40–44.

Wanga, L., Gaoa, Y., Xua, T., Xuea, Q., 2006. Acomparative study on the tribological behavior of nanocrystalline nickel and cobalt coatings correlated with grain size and phase structure. Mater. Chem. Phys. 99, 96–103.

Watson, S., 1990. Applications of Electroforming. Nickel Development Institute.

Winand, R., 1991. Electrocrystallization: fundamental considerations and application to high current density continuous steel sheet plating. J. Appl. Electrochem. 21, 377–385.

Winand, R., 1994. Electrodeposition of metals and alloys - new results and perspectives. Electrochim. Acta 39, 1091–1105.

Yang, J.-M., Kim, D.-H., Zhu, D., Wang, K., 2008. Improvement of deposition uniformity in alloy electroforming for revolving parts. Int. J. Mach. Tools. Manuf. 48, 329–337.